

PAPER • OPEN ACCESS

TEM turbulence in simulation and experiment in quasisymmetric and degraded-symmetry configurations of the HSX stellarator

To cite this article: J Smoniewski *et al* 2025 *Plasma Phys. Control. Fusion* **67** 095009

View the [article online](#) for updates and enhancements.

You may also like

- [Robustness of quasi-symmetry along parametric boundary variation](#)
Taegeun Jeong, Junyoung Jang, Dario Panici *et al.*
- [Phases and phase-transitions in quasisymmetric configuration space](#)
E Rodríguez, W Sengupta and A Bhattacharjee
- [Optimizing stellarators for large flows](#)
Iván Calvo, Felix I Parra, J Arturo Alonso *et al.*

TEM turbulence in simulation and experiment in quasisymmetric and degraded-symmetry configurations of the HSX stellarator

J Smoniewski^{1,2,*}, G M Weir³, M J Pueschel^{4,5,6}, K M Likin², B J Faber²,
I J McKinney^{7,2}, E Schilling², H Hillebrecht², B Geiger², J N Talmadge²
and D T Anderson²

¹ Max Planck Institute for Plasma Physics, 85748 Garching b. München, Germany

² University of Wisconsin-Madison, Madison, WI 53706, United States of America

³ Max Planck Institute for Plasma Physics, 17491 Greifswald, Germany

⁴ Dutch Institute for Fundamental Energy Research, 5612 AJ Eindhoven, The Netherlands

⁵ Eindhoven University of Technology, 5600 MB Eindhoven, The Netherlands

⁶ Department of Physics & Astronomy, Ruhr-Universität Bochum, 44780 Bochum, Germany

⁷ Radom Corporation, Pewaukee, WI 53072, United States of America

E-mail: jason.smoniewski@ipp.mpg.de

Received 11 April 2025, revised 13 August 2025

Accepted for publication 22 August 2025

Published 4 September 2025



CrossMark

Abstract

The Helically Symmetric Experiment (HSX) has demonstrated reduced neoclassical transport and flow damping with quasisymmetry, but the difference of turbulent transport between quasisymmetric and degraded-symmetry configurations has not been definitively assessed. Profile analysis presented here shows that anomalous transport at the mid-radius is larger with degraded quasisymmetry when temperature and density profiles are matched. An initial comparison ($T_i/T_e = 1$) between the quasisymmetric and degraded symmetry configurations finds that trapped-electron mode (TEM) turbulence can support larger heat fluxes in the degraded symmetry configuration despite smaller linear growth rates. However, further simulations at the experimental temperature ratio ($T_i/T_e = 0.2$) do not reproduce this effect. Experimental measurements of heat transport and density fluctuation amplitude are compared to nonlinear gyrokinetic simulations at the experimental temperature ratio. The heat flux and density fluctuation amplitude in simulation reproduce a substantial dependence on the density gradient, and the simulated heat flux matches measurements within experimental uncertainties, indicating that TEM turbulence is responsible for the anomalous transport at the steep density gradient in HSX.

* Author to whom any correspondence should be addressed.



Original Content from this work may be used under the terms of the [Creative Commons Attribution 4.0 licence](https://creativecommons.org/licenses/by/4.0/). Any further distribution of this work must maintain attribution to the author(s) and the title of the work, journal citation and DOI.

Keywords: stellarator, HSX, quasisymmetry, gyrokinetics, validation, TEM, reflectometry

1. Introduction

In a stellarator, where the magnetic field is entirely generated by external coils, designers have more control to impose choices on the plasma geometry than in more self-organized confinement devices. Increasingly powerful computers and numerical tools have led to the development of optimized stellarators, where the plasma boundary of a target geometry is modified in order to meet specific physics-based design goals. Optimization to reduce neoclassical transport has been successfully demonstrated in Wendelstein 7-AS [1], the Helically Symmetric eXperiment (HSX) [2], and Wendelstein 7-X [3]. With the reduction of neoclassical transport, turbulence is the dominant source of energy and particle transport across most of the radial domain in these devices.

Just as neoclassical transport can be minimized by geometry optimization, a similar strategy can target turbulent transport [4]. However, few studies have tested whether turbulence simulations accurately predict the transport in stellarator experiments, a process called validation. Validation compares a code (and underlying model) to experimental results to determine whether they are adequate to represent the relevant physics [5–7]. This effort increases confidence in the predictive ability of simulation, and identifies deficiencies for additional study and model improvement. While optimization commonly focuses only on heat or particle fluxes driven by turbulence, well-designed validation studies measure two or more quantities to reduce the likelihood of fortuitous agreement and further constrain matching simulations. Validation has become an important part in the field of turbulence simulation on the tokamak, but is still mostly absent on the stellarator.

Validation is complicated in non-axisymmetric geometry by the larger computational cost of simulations and the greater complexity of synthetic diagnostics. In an axisymmetric magnetic configuration, every magnetic field line samples the full magnetic flux surface and has identical stability properties to other field lines in that surface, allowing a reduced computational domain to represent any location on the flux surface. Particularly in the case of low shear, more common to stellarators, simulations require much higher resolutions as modes can be extended farther in the parallel direction [8]. Linear calculations can be performed at moderate computational cost, and comparisons have been made to experimental measurements [9, 10]. However, most diagnostics require solutions of the quasi-stationary saturated turbulence at the diagnostic measurement location. It is thus necessary to align the simulation domain and diagnostic lines-of-sight in order to compare against synthetic turbulence diagnostics. Nonlinear gyrokinetic simulations show that turbulent fluxes can be modified through magnetic-field-configuration changes [11–13], and initial comparisons have been made to experimental measurements [14, 15]. However, major stellarator validation studies can address the problem of co-locating measurements

and simulations by using simulations of the entire plasma volume [16], greatly increased diagnostic coverage [17], or targeted optimization of the diagnostic location and view.

The present work describes a comparison of trapped electron mode (TEM) turbulence in two configurations of a quasi-symmetric stellarator through experimental measurements and nonlinear gyrokinetic simulations. The configuration flexibility at HSX, discussed in section 2, provides an opportunity to predict how turbulent transport changes in quasi-symmetric and non-symmetric geometry, while matching the experimental conditions between configurations as closely as possible. Section 3 will present measurements of heat transport and density fluctuations and section 4 will present TEM simulations using the GENE code [18]. In order to compare to previous gyrokinetic studies for HSX, the initial comparison of the quasi-helical symmetry (QHS) and Mirror configurations in section 4.1 eliminates the temperature gradient drive and uses $T_i/T_e = 1$. Section 4.2 explores the effect of a finite temperature gradient and $T_i/T_e \neq 1$, while simulations at experimental parameters are presented in section 4.3 before being compared to the experiment in section 5. A summary of key results is provided in section 6.

2. The QHS and Mirror configurations in HSX

The HSX [19] is a stellarator designed to demonstrate the feasibility and benefits of QHS, a symmetry in the magnitude of the magnetic field B , but not necessarily in the vector \mathbf{B} . The magnitude of the magnetic field on a flux surface can be represented by a Fourier expansion as

$$\frac{B}{B_0} = 1 + \sum b_{nm} \cos(n\phi - m\theta). \quad (1)$$

Here, B_0 is the average magnetic field on the surface, n and m are the toroidal and poloidal mode numbers, and ϕ and θ are the toroidal and poloidal coordinates, respectively. In Boozer coordinates, the magnetic spectrum in a quasi-symmetric stellarator is dominated by a single mode b_{nm} , causing the collisionless bounce-averaged drift of trapped particles from a flux surface to become small and thus reducing neoclassical transport and flow damping [20].

In the HSX stellarator, a set of 48 modular coils produces a four-field-period ($n = 4$, $m = 1$) quasi-helically symmetric magnetic field $B = 1$ T [21], as seen in figure 1. A set of planar auxiliary coils can be energized to modify the magnetic spectrum, introducing non-symmetric terms similar to a conventional stellarator. This configuration flexibility has allowed experiments to directly compare quasisymmetry to a variety of degraded-symmetry configurations, the most studied of which add $m = 0$ mirror terms to the spectrum. The Mirror configuration, developed in [22], degrades quasisymmetry by adding large $(4, 0)$ and $(8, 0)$ modes to the spectrum with little effect

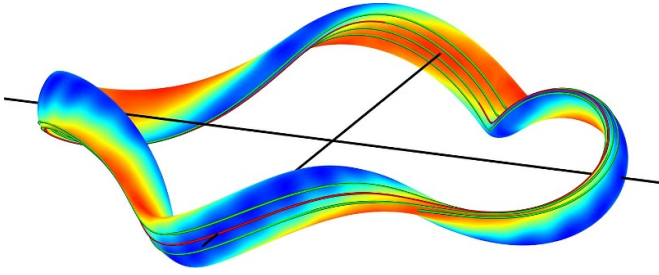


Figure 1. A flux surface and field line for the QHS configuration of HSX. Colors correspond to $|B|$, where blue is the minimum field strength. A field line followed for one poloidal turn is shown in red, and its extension to four poloidal turns is shown in green.

on other parameters known to affect anomalous transport, such as the plasma volume, rotational transform, and magnetic well depth [23]. Experiments have previously demonstrated that flow damping [24] and neoclassical transport [2] are reduced in the standard QHS configuration by comparing to these degraded-symmetry configurations. Of particular interest to this work, it has been suggested that optimization for neoclassical transport can also reduce turbulent transport through the reduced damping of zonal flows [25].

While neoclassical transport is reduced in QHS, anomalous transport dominates the energy flux in both QHS and Mirror outside the innermost plasma core region [2]. This is particularly true for $r/a > 0.3$, where the temperature profile is flatter and the density gradient peaks. The dominant instability in HSX is the TEM, driven by the density gradient and destabilized by overlap of particle trapping (minimum $|B|$) and bad curvature ($\kappa_n < 0$) regions [12, 26, 27]. The additional mirror terms in the magnetic spectrum of the Mirror configuration increase the trapped-particle fraction, but also increase the magnetic field in particle trapping regions, reducing the overlap of particle trapping and bad curvature. This is seen in the central magnetic field minimum at $\theta = 0$ in figure 2 for a field line from the radial location $r/a = 0.7$, where $r/a = \sqrt{\Psi/\Psi_0}$, Ψ/Ψ_0 is the normalized toroidal flux, and a and Ψ_0 are the average minor radius and toroidal flux at the last closed flux surface. Typical TEMs peak strongly near $\theta = 0$, often making this central minimum the most important for prediction. However, the low- k_y modes in HSX tend to be broad and sample many other magnetic minima where the overlap between particle trapping and bad curvature may not be reduced. Notably, the Mirror configuration is a more elongated configuration than QHS, which has been shown to reduce the growth rates of long-wavelength modes provided the QHS is approximately conserved [28].

Early computational studies of the TEMs in HSX yielded contradictory results of smaller [26] or larger [29] linear growth rates in the Mirror configuration than in QHS, but their simulation setup has been superseded by code developments since. Experimental measurements of density fluctuation amplitudes, correlation lengths, and particle flux did not find a significant difference between configurations [30]. Nonlinear gyrokinetic simulations confirmed that ∇n -driven TEM turbulence is expected in the QHS configuration, and

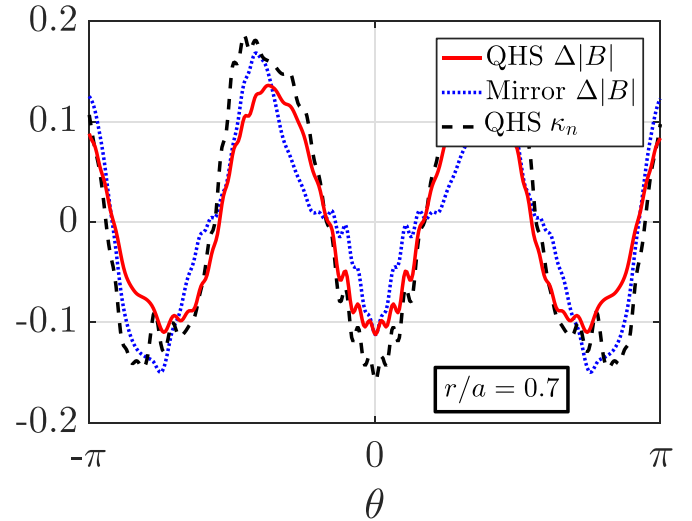


Figure 2. Comparison of the variation of the magnetic field $\Delta|B| = B - B_0$ in the QHS and Mirror configurations along a field line, where θ is the poloidal coordinate. The local curvature κ_n is nearly identical in QHS (shown) and Mirror.

identified a double peak in the flux spectra that is not predicted by the linear growth rates [11], but did not investigate the Mirror configuration. An earlier comparison between experimental transport on HSX and nonlinear simulations of TEM turbulence found that the simulated heat flux driven by the TEM was an order of magnitude larger than the experimental heat flux [14]. However, these simulations did not match the experimental temperature gradient a/L_{Te} or temperature ratio T_i/T_e , and further simulations demonstrated that extended flux tubes are needed to properly resolve eigenmodes and turbulence in low-shear devices such as HSX [8]. By taking into account these factors, the present effort employs a state-of-the-art gyrokinetic flux-tube simulation setup to make meaningful quantitative comparisons with the experiment.

3. Experimental measurements

Section 3.1 examines energy transport in the QHS and Mirror configurations for comparison to simulation. While discharges are directly compared by matching the absorbed power or density profile in the following paragraphs, the remainder of this study examines the scaling of heat flux with driving gradients. A reduced model of the power balance in HSX plasmas is used to calculate the heat flux for a large number of profiles within a range of driving gradients. Turbulence simulations are sensitive to input parameters such as driving gradients, and experimental measurements of those gradients involve large uncertainty. Reflectometry measurements of the density fluctuation amplitude in the QHS and Mirror configurations are reported in section 3.2 to reduce the chances of finding accidental agreement based on turbulent transport alone. This diagnostic has the advantage of being most sensitive at steep density gradients, precisely where the ∇n -driven TEM is expected to be most unstable. In section 5, experimental

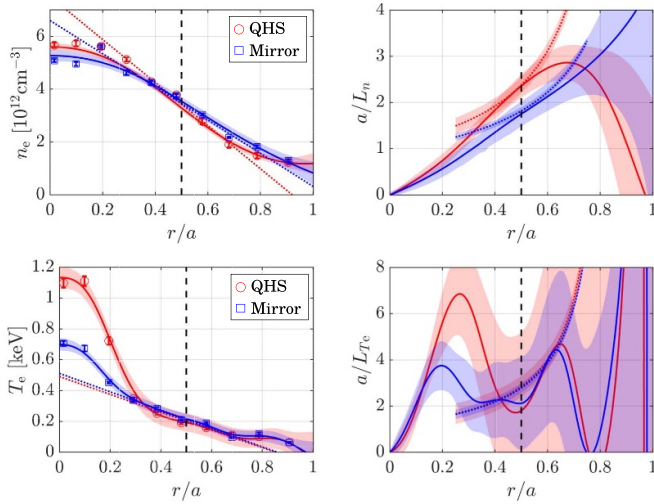


Figure 3. Temperature and density profiles and their normalized gradients when the absorbed ECRH power $P_{\text{abs}} = 18 \pm 3$ kW is the same in both the QHS (red) and Mirror (blue) configurations. Measurements from Thomson scattering are plotted as symbols. GPR is used to produce a smooth fit to the experimental data, and dotted lines correspond to a linear fit for the region $0.3 \leq r/a \leq 0.7$. The shaded regions are the 1σ uncertainty of the fits. The vertical dashed lines mark the reflectometry measurement location. The temperature gradient peaks at $r/a \lesssim 0.3$, while the density gradient is largest for $r/a > 0.5$.

measurements from this section will be compared to simulations from section 4.

Plasmas are heated by up to 100 kW of electron cyclotron resonance heating (ECRH), while ions are heated only by collisions. Typical line-averaged plasma densities are $4 \times 10^{12} \text{ cm}^{-3}$, and core temperatures can reach 2 keV. Example profiles of the electron temperature and density from Thomson scattering are shown in figure 3. The radial coordinate ρ is defined as $\rho = r/a = \sqrt{\Psi/\Psi_0}$. Density and temperature gradients are normalized as a/L_n and a/L_{Te} , where $L_n^{-1} = -\nabla \ln n$ and $L_{Te}^{-1} = -\nabla \ln T_e$. At the time of these measurements, the HSX Thomson scattering diagnostic required 2 – 12 reproducible plasma discharges to accumulate sufficient photon statistics. This diagnostic provides measurements of the electron density n_e and temperature T_e at 10 points across the minor radius [31, 32]. While a Gaussian process regression (GPR) tool [33] is used to fit some profiles, as seen in figure 3, a linear fit adequately represents the profile data in the mid-radius region of interest for reflectometry $0.3 \leq r/a \leq 0.7$. The linear fit is used here to quickly and robustly calculate gradients for a large number of profiles.

A database of 200 profiles has been collected consisting of 1435 plasma shots. The distribution of gradients in the database is shown in figure 4, where it is evident that both gradients a/L_n and a/L_{Te} tend to be larger in QHS than in Mirror profiles. It is not clear if this is a physical effect, or due to sampling bias from the fact that experimental operations have more fully explored the QHS operation space, and operators are more equipped to achieve higher performance in QHS. The database can be filtered by any standard measurements at HSX, such as n_e , T_e , and absorbed power P_{abs} , to find similar plasma

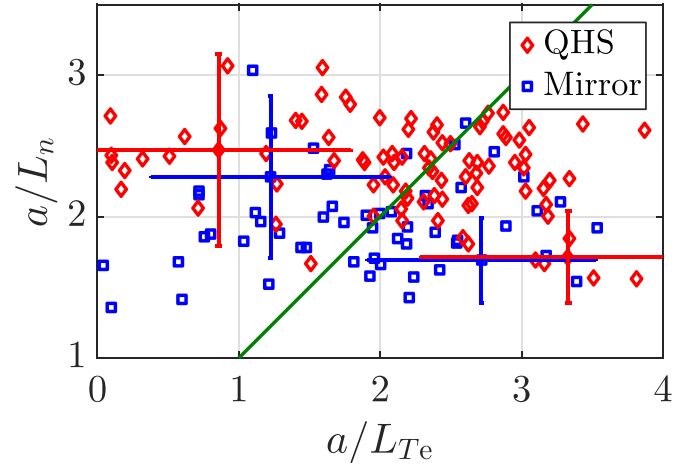


Figure 4. The distribution of gradients in the HSX profile database at $r/a = 0.5$ for QHS (red diamonds) and Mirror (blue squares). Select points are drawn with a representative uncertainty. The straight green line corresponds to $a/L_{Te} = a/L_n$.

profiles. Further filtering can select narrow ranges of a/L_n or a/L_{Te} to compare the scaling of a measurement with driving gradient. The profiles in figure 3 were found by filtering the database for QHS and Mirror profiles with the same absorbed power $P_{\text{abs}} = 18 \pm 3$ kW. The QHS profile comes from shots [39, 42, 49, 54, 62, 68] on 2012-05-08, and the Mirror profile comes from shots [59, 60, 61, 62, 63] on 2014-06-24. As seen in figure 3, the temperature is typically more peaked towards the magnetic axis, and the mid-radius density gradient is larger in QHS as compared to Mirror. Efforts to match profiles use less heating power in the QHS configuration to compensate, but have struggled to match core temperature, core density, and profile gradients between configurations. The database compiled for the present work has enabled matching profiles between QHS and Mirror across the entire minor radius to within experimental uncertainties, as seen in figure 5. The Mirror profile is the same as in figure 3, and the QHS profile comes from shots [87, 88, 91, 92, 93, 94, 95] on 2010-10-08, where the absorbed power $P_{\text{abs}} = 9 \pm 2$ kW and the magnetic field was in the opposite direction.

Analysis in section 3.1 and measurements in section 3.2 target the mid-radius $r/a = 0.5$, where anomalous transport and the normalized density gradient are both large. The large density gradient provides the best localization for reflectometer measurements, whereas other regions face various measurement or simulation challenges. Deep in the core of the plasma, density gradients are small, and the large temperature gradient may make the ETG mode important [14], which exists at scales too small to be measured by current diagnostics on HSX. Within $r/a \lesssim 0.3$, neoclassical calculations predict very strong $E \times B$ shearing that could have a suppression effect on turbulence, possibly complicating interpretation of the TEM turbulence [27]. However, this core electric field shearing has not been observed experimentally. For $r/a > 0.3$, the electric field is measured to be relatively constant with very little shear [34, 35], and is not expected to affect turbulence. Towards the edge, at $r/a > 0.8$, the low density and temperature in HSX

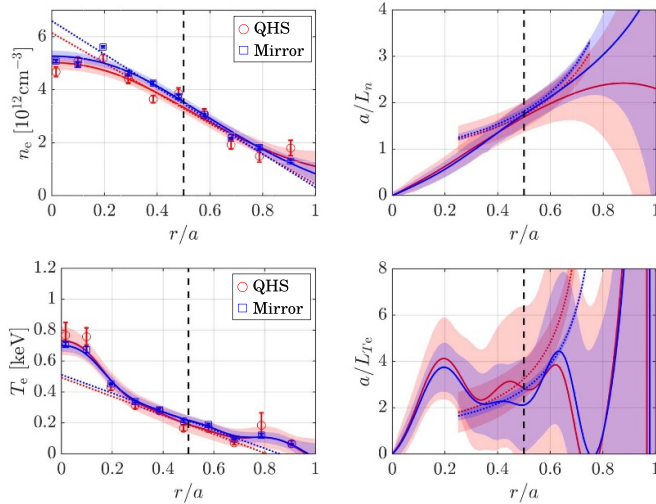


Figure 5. The HSX profile database enables matching of QHS and Mirror profiles to within experimental uncertainties. Data from Thomson scattering is plotted as points, and GPR is used to create a smooth fit to the experimental data. The dotted straight lines correspond to linear fits in the region $0.3 \lesssim r/a \lesssim 0.7$. The vertical dashed lines mark the reflectometry measurement location. The shaded regions are the 1σ uncertainty of the linear and GPR fits.

plasmas make charge exchange and ionization important parts of transport.

3.1. Electron energy transport

This section examines the dependence of energy transport, quantified by the electron heat flux Q_e , on a/L_n and a/L_{Te} . In steady state, the flux-surface-averaged energy continuity equation for the electrons can be written as

$$\frac{1}{V'} \frac{\partial}{\partial \rho} V' \langle Q_e \cdot \nabla \rho \rangle = \sum p(\rho), \quad (2)$$

where $\rho = r/a$, $V' = dV/d\rho$, V is the volume enclosed by a flux surface, $\langle \cdot \rangle$ denotes a flux-surface average, and $\sum p(\rho)$ is the sum of all energy sources and sinks. Integrating (2) over ρ allows writing the heat flux as

$$Q_e = \frac{\int_0^\rho \sum p(\bar{\rho}) V'(\bar{\rho}) d\bar{\rho}}{V'(\rho) \langle |\nabla \rho| \rangle}. \quad (3)$$

This study calculates the heat flux Q_e for a range of similar profiles to produce a scaling of the thermal transport with driving gradients, which will be compared to simulation in section 4.

ECRH is the source of electron heating in HSX. While energy is lost due to radiated power, ionization, and electron-ion collisions, these account for a small fraction of the absorbed power. For the profiles in figures 3 and 5, the radiated power measured by bolometers viewing the entire cross-section is 3–4 kW, and most of that power is radiated in the plasma periphery [29]. Particle transport calculations in previous studies estimate that ionization accounts for ≈ 1 kW within $r/a \lesssim 0.6$, and the power transfer to ions due to collisions between electrons and 50 eV hydrogen ions is ≈ 1 kW

within $r/a < 0.6$ [29]. These energy losses are on the order of the uncertainty of the measured P_{abs} and are neglected here. Ray-tracing calculations show that power deposition from ECRH takes place entirely within $r/a \lesssim 0.3$ [36]. By calculating the heat flux outside the power deposition region for gradient scans, the numerator in (3) reduces to the total absorbed power P_{abs} , and the heat flux becomes

$$Q_e = \frac{P_{\text{abs}}}{V' \langle |\nabla \rho| \rangle}, \quad (4)$$

where the geometric terms come from field-line following calculations of the vacuum magnetic geometry at $r/a = 0.5$ where $V' \langle |\nabla \rho| \rangle = 3.898$ in QHS and $V' \langle |\nabla \rho| \rangle = 3.801$ in Mirror.

Typical QHS profiles have higher core electron temperatures and steeper mid-radius density gradients than comparable Mirror plasmas, as seen in figure 3. Generally, TEMs can be driven by temperature and density gradients. Therefore, a matched-profile experiment between the QHS and Mirror configurations, presented in figure 5, is used to prevent differences in gradient drive. The heat fluxes for both these profiles are plotted in figure 6, along with calculations of neoclassical transport from the PENTA [37, 38] code. The ion root (circles in QHS, squares in Mirror) is present across most of the minor radius, and approaches the experimental heat flux in the core. Deeper in the core, there is an electron root (stars in QHS, crosses in Mirror) that drives very little flux. Inside $r/a \lesssim 0.3$, the heat flux is reduced in the QHS configuration as compared to Mirror, a consequence of reduced neoclassical transport. This region has been thoroughly investigated in earlier work [2, 14, 29, 39], and is not the focus of the present study. Outside $r/a \gtrsim 0.3$, the experimental heat flux is much larger than the neoclassical heat flux. There, neoclassical electron heat flux is small and trending downward proceeding outward from $r/a = 0.35$ and cannot account for the difference between the QHS and Mirror configurations. The neoclassical transport provides a very small contribution to the overall thermal transport at $r/a = 0.5$ [39] and will be neglected in the following.

When P_{abs} is matched between QHS and Mirror, a/L_n is larger in the QHS configuration. When profiles and gradients are matched, the heat flux is smaller in QHS. The difference in $V' \langle |\nabla \rho| \rangle$ between configurations is small, implying that this larger flux is due to a difference in P_{abs} , the only measured quantity in (4). Less power is required to sustain the same profile in the QHS configuration than in Mirror, matching previous results [2]. The difference between the experimental and neoclassical electron heat fluxes is expected to be turbulent electron heat flux driven by the TEM. While the electron temperature gradient peaks in the core, the anomalous electron heat flux is larger at the mid-radius, where the density gradient is largest. This supports the idea that the TEM is primarily driven by the density gradient in HSX.

While the energy transport analysis in figure 6 shows that the electron heat flux is larger in the Mirror configuration when profiles are matched, analysis of multiple profiles produces a scaling of the thermal transport with driving gradients, which

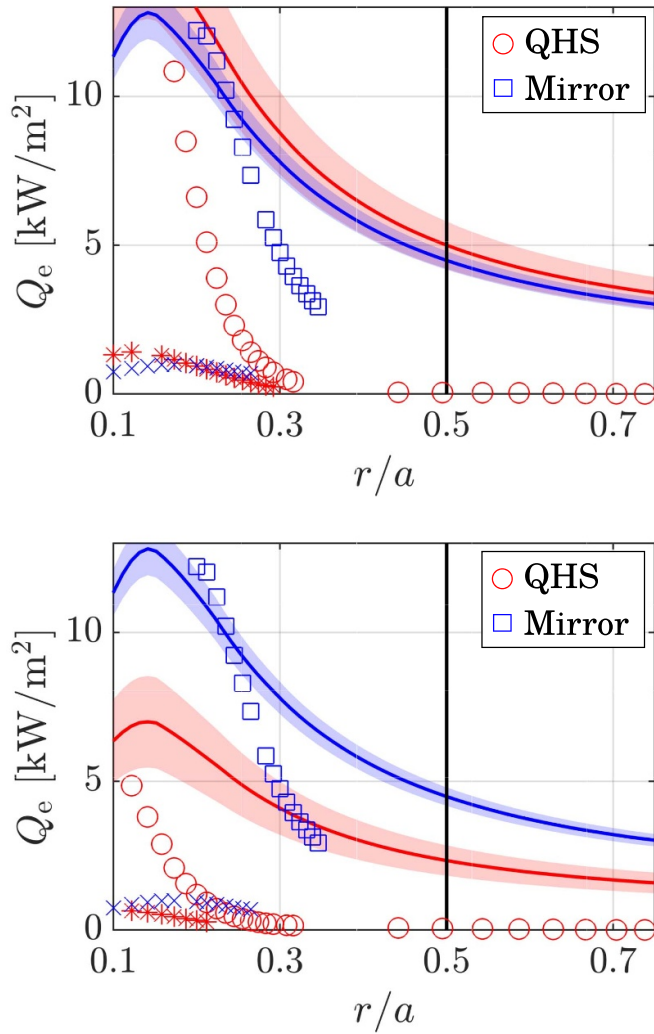


Figure 6. The heat flux (solid lines) for profiles with the same P_{abs} (top, from figure 3) and matched profiles (bottom, from figure 5) compared to neoclassical calculations. The indicated uncertainty in Q_e is solely due to uncertainty in P_{abs} . In neoclassical calculations, two ambipolar roots exist in the core: the ion root (circles in QHS, squares in Mirror), and the electron root (stars in QHS, crosses in Mirror) [37].

will be compared to simulation in section 4. Here, the profile database is filtered to find similar plasma profiles across a range of density or temperature gradients. One gradient can be scanned while holding the other approximately constant. While the uncertainties in a/L_n , a/L_{Te} , and Q_e are large for an individual profile, this analysis captures the trend. Experiments with large gradient uncertainties $\delta(a/L_{n,T}) > 2$ or large uncertainties in the absorbed power are removed from the dataset prior to analysis. Filters on the electron temperature and power-per-particle P_{abs}/n_e eliminate outliers from the analysis.

The electron heat flux across a scan of the density gradient is shown in figure 7. Profiles have been selected for $1.7 < a/L_{Te} < 2.8$, which is approximately equal to the typical uncertainty in a/L_{Te} . Due to the difficulty to achieve higher density gradients in Mirror, there is not enough data to

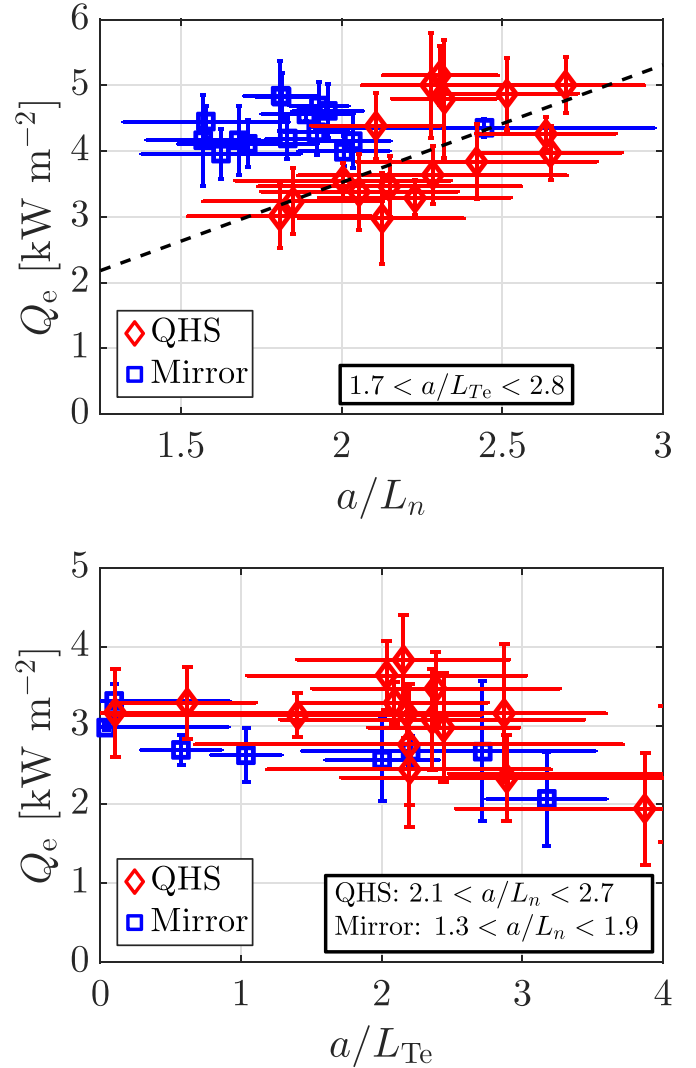


Figure 7. The scaling of the electron heat flux Q_e with density gradient a/L_n (top) and temperature gradient a/L_{Te} (bottom) at $r/a = 0.5$. A linear fit (dashed line) shows that the heat flux in QHS increases with a/L_n . The temperature gradient scaling uses different a/L_n filters in the QHS and Mirror configurations due to the profile distribution in figure 4.

determine a scaling in that configuration. However, the heat flux in QHS increases from 3kW to 5kW across a change in a/L_n of 0.5. Where Mirror data is available, Q_e is larger than in the QHS configuration, possibly related to the larger density n_e in Mirror profiles required to match a/L_n . A similar scan of the temperature gradient is also shown in figure 7. Mirror profiles are generally distributed over lower density gradients, as seen in figure 4, and thus different gradient filters were used for the QHS and Mirror profiles. For these filters, the heat flux is similar in QHS and Mirror, despite a significantly smaller density gradient in the Mirror profiles. In both configurations, the heat flux is roughly independent of the temperature gradient. Together, the scaling with density gradient and lack of scaling with temperature gradient are indicative of predominantly ∇n -driven turbulence.

3.2. Density fluctuation measurements from reflectometry

Local measurements of density fluctuations by reflectometry have successfully compared to gyrokinetic calculations in other studies [16, 40, 41] and complement the global energy transport measurements in section 3.1. Fluctuations are measured with a profile reflectometer mounted at the midplane on the high-field-side of the bean-shaped cross section of HSX [42]. The radial localization is determined from the cutoff density for ordinary-wave-polarized microwaves calculated assuming a cold plasma [43], and the probe beam frequency is stepped between 15 and 26 GHz to scan across the plasma radius. The simulation domain described in section 4 matches the cross section and poloidal location sampled by the reflectometer with a beam diameter of ~ 8 cm at $r/a \approx 0.5$, sensitive to fluctuations in the range $0.2 \lesssim k_{\perp} \rho_s \lesssim 1$, where k_{\perp} is the mode number perpendicular to the field line, and ρ_s is the ion sound gyroradius $\rho_s = \sqrt{T_e m_i c / (e B_0)}$, where c is the speed of light, e is the elementary charge, and B_0 is the magnetic field on axis.

In the simplest interpretation, fluctuations in the phase of a reflected microwave beam correspond to radial fluctuations of the cutoff layer and are linearly related in amplitude to density fluctuations at that layer. However, significant refraction or large fluctuation amplitudes can complicate the linear relationship, leading to saturation of the beam phase fluctuations and decoupling from the density fluctuations of the cutoff layer. In that case, the standard deviation of the reflected power would be comparable to the total reflected power and the measured phase would be evenly distributed between $-\pi$ and π . HSX measurements do not show either of these indicators of saturated reflectometry measurements. A nonlinearity parameter $\gamma > 1$ indicates when significant nonlinear effects are expected [44]. The nonlinearity parameter is

$$\gamma = \left(\frac{\delta n}{n} \right)^2 \frac{G^2 \omega_b^2 x_c l_{cx}}{c^2} \ln \frac{x_c}{l_{cx}}, \quad (5)$$

where $G = 1$ in the ordinary-mode polarization, x_c is the distance traveled inside the plasma to the cutoff layer, l_{cx} is the turbulent radial correlation length, and c is the speed of light [45]. For measurements at $r/a = 0.5$, the beam frequency $\omega_b = 2\pi \cdot 19$ GHz and $x_c = 6$ cm. Simulations from section 4 using plasma parameters from $r/a = 0.5$ predict amplitudes $\delta n/n \approx 0.04$ and $l_{cx} \approx 0.5$ cm, while previous measurements at $r/a = 0.8$ and low density find $\delta n/n \approx 0.2$ and $l_{cx} \approx 0.5$ – 1.5 cm, both decreasing with increasing density towards the core [30]. For conservative estimates of $\delta n/n \approx 0.05$ and $l_{cx} \approx 1.5$ cm, the nonlinearity parameter is $\gamma \approx 0.5$; hence the fluctuation amplitude is indeed expected to be linearly related to fluctuations in the reflected beam. Results here find the fluctuation amplitude to be smaller than this estimate ($\delta n/n \approx 0.01$), and a reduction of the correlation length would only reduce γ further.

Density fluctuations can be modeled as a radial perturbation to the reflecting layer. At small amplitude, the radial displacement ϵ of the reflecting layer is directly related to fluctuations

of the measured phase on the order of [46]

$$\phi_{sd} = \frac{4\pi\epsilon \cos \theta_1}{\lambda \sqrt{2}} \left(\frac{k_w w}{2\pi} \right)^{-0.6}. \quad (6)$$

Here, ϕ_{sd} is the standard deviation of the measurement of the phase, ϵ/λ is the radial dimension of fluctuations normalized to the wavelength of the probe beam, θ_1 is the incident angle of the probe beam, k_w is the spectral half-width of the fluctuations, and w is the beam radius. For a normal-incident probe beam, as in HSX, $\theta_1 = 0$. The spectral half-width assumes a Gaussian distribution with respect to fluctuation wavenumbers, and simulations in section 4 estimate $k_w \approx 1/\rho_s$. While ϕ_{sd} is measured in the experiment, fluctuations are normalized as $\delta n/n$ for comparison to simulated turbulence. By using the relation to $\delta n/n$ [47]

$$\frac{\delta n}{n} \approx \frac{\epsilon}{n} \frac{dn}{dr} \Big|_{n=n_c}, \quad (7)$$

the normalized density fluctuations measured by the reflectometer can be written as a function of the measured density gradient and the standard deviation of the phase fluctuations as

$$\begin{aligned} \frac{\delta n}{n} &\approx \left[\frac{\lambda \sqrt{2}}{4\pi a} \left(\frac{k_w w}{2\pi} \right)^{0.6} \right] \phi_{sd} \left(\frac{1}{n} \frac{dn}{d\rho} \right) \Big|_{n=n_c} \\ &\approx 0.0464 \phi_{sd} \left(\frac{1}{n} \frac{dn}{d\rho} \right) \Big|_{n=n_c}. \end{aligned} \quad (8)$$

This reflectometry model has not been validated against experimental data, and the absolute value of reflectometry fluctuations should only be viewed with caution. However, the model is sufficient to compare density fluctuations between discharges, and can adequately capture the trend with changing gradients.

A subset of profiles in the database with reflectometry measurements available are plotted in figure 8, without filtering by gradients. While there is insufficient QHS data alone to describe a trend, the sum of QHS and Mirror data shows that density fluctuations increase with the density gradient. From the simulations in section 5, a significant difference in fluctuation amplitudes is not expected between QHS and Mirror. In both configurations, no relationship is found between density fluctuations and the temperature gradient. This dependence on the density gradient, and not the temperature gradient, is consistent with fluctuations driven by an instability destabilized by the density gradient.

Density fluctuations typically increase with the background density, as shown for HSX in figure 9. While profiles analyzed for reflectometry have not been filtered for matched density, fluctuations are larger in the QHS configuration across the density range. This can be explained by figure 8, where a/L_n is larger in the QHS data. Therefore, density fluctuations depend on the density and the density gradient, which tend to be correlated, rather than solely on the background density.

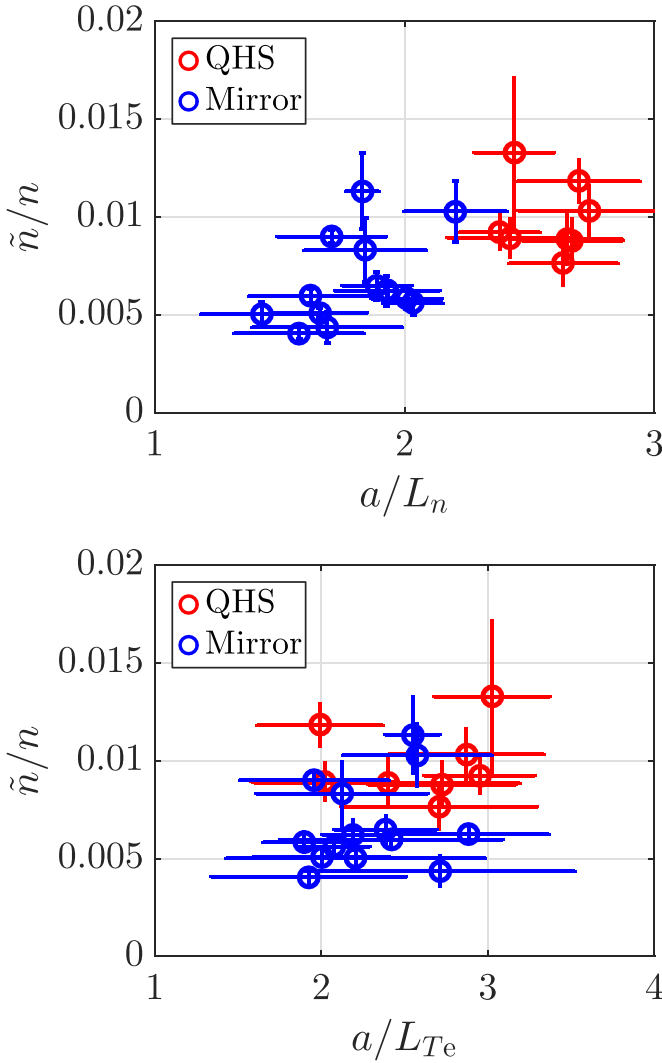


Figure 8. The sum of QHS and Mirror data shows that density fluctuations increase with density gradient, but there is insufficient data to describe a trend for either configuration individually (top). Both configurations show no dependence on the temperature gradient (bottom).

4. Simulation of TEM turbulence in QHS and Mirror

This section examines the dependence of linear growth rates and nonlinear heat flux in gyrokinetic simulations on the driving gradients a/L_n and a/L_{T_e} . Throughout, comparisons are made between the QHS and Mirror configurations. The ∇n drive of the TEM is expected to be more important than the ∇T_e drive around the mid-radius of HSX. Therefore, the initial comparison in section 4.1 isolates the ∇n effect by eliminating the temperature gradient and using $T_i/T_e = 1$. These parameters are chosen to compare to previous gyrokinetic studies for HSX. Important for an experimental comparison, the effect of including the experimental temperature ratio is described in section 4.2. Finally, simulations at experimental parameters that scan the density and temperature gradients are presented in section 4.3 to be compared to the experimental measurements. The first point of comparison between configurations will be linear calculations, which are used to obtain growth

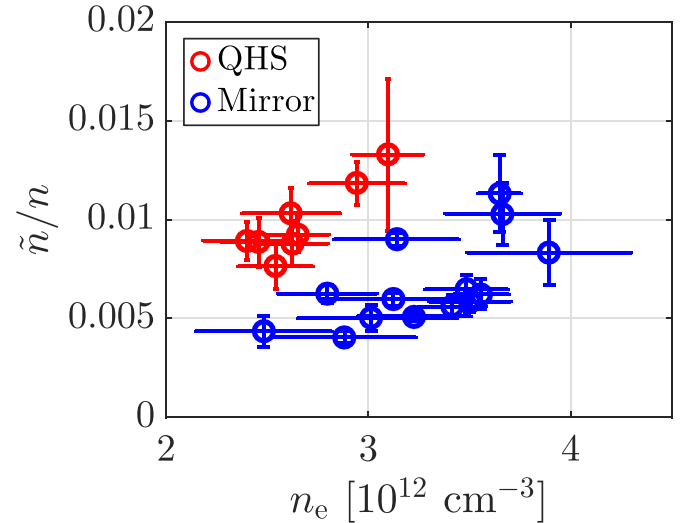


Figure 9. Density fluctuations increase with increasing background density n_e . While fluctuations are larger in QHS, note that a/L_n is larger in QHS, as seen in figure 8.

rates, frequencies, and eigenmode structures. Nonlinear simulations of saturated turbulence are then used to compare heat and particle fluxes, and density fluctuation amplitudes.

These simulations use the GENE code [18], a gyrokinetic δf continuum code. GENE can be used to solve the linearized gyrokinetic Vlasov equation to describe individual eigenmodes, or for nonlinear simulations of, typically, quasi-stationary turbulence. While equilibria typically depend on the plasma pressure, vacuum fields are used here, which is consistent with the low normalized plasma pressure ($\beta < 0.1\%$ for $r/a > 0.2$ in HSX). The magnetic geometry studied here is a flux tube, calculated with the GIST code [48] from VMEC equilibria [49]. A flux tube is a reduced-geometry representation for, e.g. toroidal magnetic geometries [50], and is constructed from a sheared box around a single field line identified by a field-line label $\alpha = (\sqrt{s}/q)(q\theta^* - \phi)$ in PEST [51] coordinates, where s is the normalized toroidal flux, $q = 1/t$ is the safety factor, ϕ is the toroidal angle, and θ^* is the straight-field-line poloidal angle. The box uses non-orthogonal coordinates x in the radial direction, y in the flux surface, and z along the field line. In a GENE flux tube, spectral representation is used for the x and y directions, with wavenumbers k_x and k_y normalized as $k_{x,y}\rho_s$, while the quasi-periodic z direction is resolved in real space. The local representation does not permit inclusion of the radial electric field, only of radial electric-field shear. While electric-field shear can suppress turbulence, the ambipolar electric field in HSX is about 5 kV m^{-1} with little shear across the minor radius [34, 35], and thus is neglected in these simulations.

The radial box size of a flux tube is a function of the magnetic shear through the ‘twist-and-shift’ boundary condition as $L_x = N/(\hat{s}k_{y,\min}n_{\text{pol}})$, where \hat{s} is the normalized average magnetic shear, $k_{y,\min}$ is the smallest finite y -wavenumber in the simulation, n_{pol} is the parallel length of the flux tube in number of poloidal turns, and the integer N determines the aspect ratio of the computational domain. In HSX, the shear is very

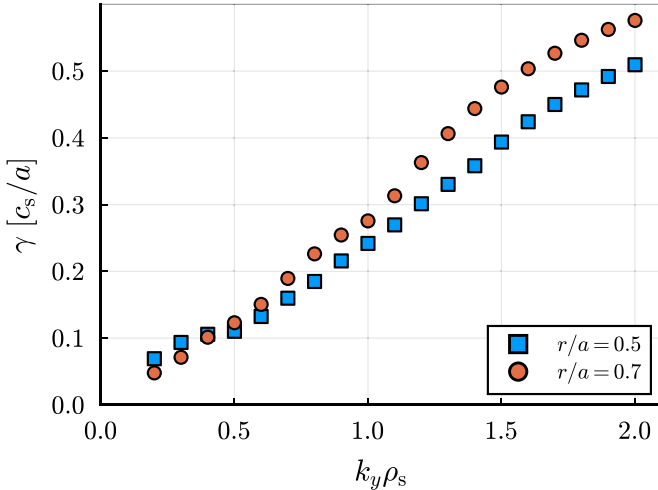


Figure 10. A comparison of the growth rates in the QHS configuration for flux tubes at two radial locations. ($a/L_n = 2$, $a/L_{Te} = 2$, $T_i/T_e = 0.2$).

small, $\hat{s} \approx -0.05$ at $r/a \approx 0.7$, and simulations require large radial domains. For simulations here, the small shear also implies that flux tubes need to be extended to multiple poloidal turns, as discussed in [8] and [52]. Other boundary conditions have been developed but show no significant difference to the ‘twist-and-shift’ boundary when extended to many poloidal turns [53], as was used here.

In part due to the small average shear in HSX, changes in the magnetic geometry are relatively small across a large fraction of the minor radius. In order to mitigate the considerable computational effort due to the resolution requirements at $r/a = 0.5$ where the shear is even smaller, and to facilitate comparison with previous work, a flux tube from the $r/a = 0.7$ flux surface is used for simulations here. A previous study using a zero-shear approximation showed convergence with the finite-shear flux tubes used here [8], indicating that the small difference in shear between radial locations is unlikely to affect the instability drive. In addition, the fraction of trapped particles increases with radius. This could increase growth rates in the flux tube at the larger radius, which is confirmed in figure 10. However, differences between growth rates are generally small and suggest that using the $r/a = 0.7$ flux tube should be sufficient for the purposes of the comparison in this paper.

In perfectly axisymmetric tokamaks, every flux tube on a given flux surface is identical, and a single flux tube can be expected to capture the physics on the entire surface. Each flux tube in a stellarator is generally unique, and a local simulation will not always capture surface-averaged transport. However, quasi-stationary transport for the flux surface is found to lie between that of the highest- and lowest-transport tubes for Wendelstein 7-X [54]. For HSX, the flux from different flux tubes was found to converge as flux tubes are extended to four poloidal turns. Simulations here use the flux tube centered on the outboard midplane of the bean-shaped cross section ($\alpha = 0$), where the magnetic-trapping

and bad-curvature regions overlap. The flux tube is extended to four poloidal turns, and convergence was checked with eight and sixteen poloidal turns. Typical resolutions for nonlinear simulations use $N_x \times N_y \times N_z \times N_{v_{\parallel}} \times N_{\mu} = 128 \times 32 \times 256 \times 32 \times 8$ grid points where x , y , and z are the spatial coordinates, v_{\parallel} is the velocity along the field line, and μ is the magnetic moment. Note that N_z grid points resolve the entire four poloidal turns. Simulations here are collisionless and have kinetic ion and electron species. Linear calculations use a normalized electron pressure $\beta = 0$, while $\beta = 0.0005$ in nonlinear simulations in order to avoid unnecessary time-step restrictions. The ion temperature is small in HSX, with $T_i < 70$ eV across the plasma radius, and thus the gradient a/L_{Ti} is set to zero. Hereafter, ‘temperature gradient’ refers to the electron temperature gradient.

Nonlinear simulations in HSX geometry can take substantial time to saturate, with more than one quasi-stationary state with statistically converged fluxes and fluctuation amplitudes. Due to this time evolution, a shorter time-trace is used here which may introduce further uncertainty to the simulated heat fluxes. Future analysis with GPU-based simulations should resolve the long-time evolution.

4.1. Comparison of the QHS and Mirror configurations

A previous study of TEM turbulence in the QHS geometry of HSX found that the nonlinear heat flux increased more quickly with the density gradient than would be expected from linear growth rates [11]. This section compares ∇n -driven TEM turbulence in the QHS and Mirror configurations. Moreover, both experimental [55] and numerical [14, 30] evidence suggests that the ∇n drive of the TEM is more important than the ∇T_e drive around the mid-radius of HSX. Therefore, while not comparable to the experimental measurements, the ∇T_e drive is eliminated with $a/L_{Te} = 0$ and $T_i/T_e = 1$ in this section to establish a baseline for comparison with earlier work before using more realistic parameters.

The Mirror configuration is expected to be more linearly stable to TEMs due to the reduced overlap of the trapped-particle regions and bad curvature, as discussed in section 2. The linear growth rates γ versus wavenumber k_y in figure 11 show that the QHS configuration is indeed more unstable for $k_y > 0.7$, particularly at larger a/L_n , following this expected dependence. Eigenmodes have a potential structure extended along the field line that is categorically different between branches at high or low- k_y . Higher- k_y modes tend to have a narrower eigenfunction and follow the expected dependence on the overlap of the local trapped-particle and bad-curvature regions. Low- k_y modes have a broader eigenfunction that is extended along the field line and largely insensitive to the individual trapped-particle regions. There is no significant difference between the QHS and Mirror configurations at these small wavenumbers. These results are consistent with [28], such that growth rates for $k_y > 1$ may be reduced due to the more elongated Mirror configuration, while benefits due to elongation at $k_y < 1$ are negated by the degraded quasisymmetry.

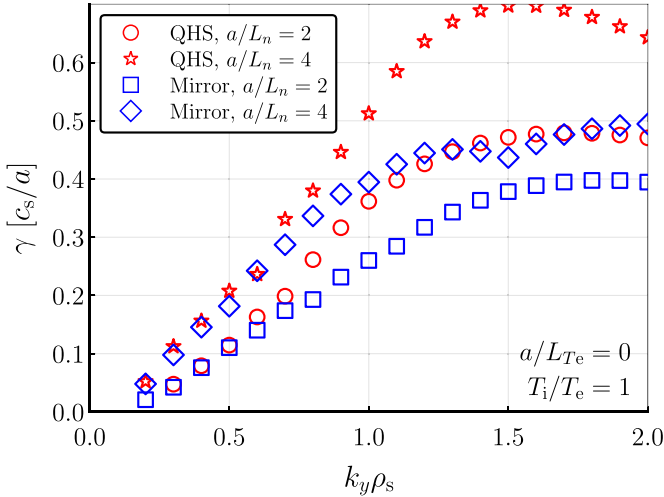


Figure 11. Linear growth rates of the most unstable mode in the QHS and Mirror configurations for $a/L_{Te} = 0$ and $T_i/T_e = 1$ at two different density gradients.

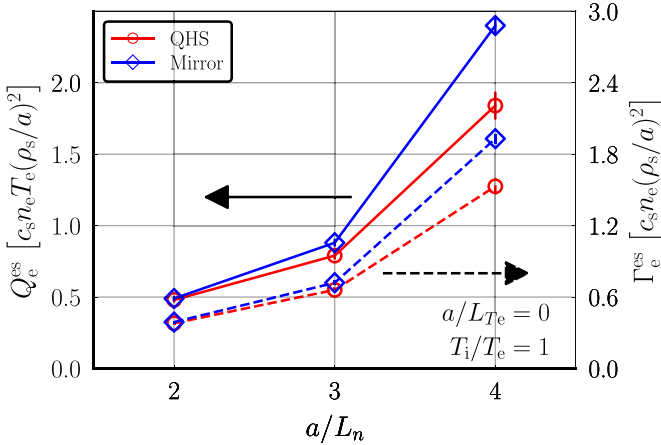


Figure 12. The heat flux (solid lines) and particle flux (dashed lines) from nonlinear TEM simulations increase strongly with a/L_n . Statistical error bars of the flux in the quasi-stationary state are indicated as vertical bars but are mostly smaller than the size of symbols.

Commonly, quasi-linear estimates $\propto \gamma k_y^2$ are seen as an indicator of transport in saturated turbulence [56], and fluxes would be expected to be larger in the QHS configuration. However, nonlinear simulations reveal qualitatively different behavior from what would be expected based on linear growth rates. The heat and particle fluxes in the QHS and Mirror configurations, presented in figure 12, scale strongly with the density gradient in both the QHS and Mirror configurations. Despite larger growth rates in the QHS configuration, both heat and particle fluxes are slightly larger in the Mirror configuration at higher density gradients. Here, no difference is found in the dependence of the heat compared with the particle fluxes on the gradient, and either flux is a good indicator of TEM turbulence activity. Comparing with the linear trend in figure 11, the growth rate of the most unstable mode is not a good proxy for transport, the same result as a comparison between ion temperature gradient (ITG) turbulence in

quasi-helically symmetric and quasi-axisymmetric stellarators [57]. The discrepancy between the quasi-linear expectation and the nonlinear transport may in part be due to other unstable but subdominant modes [58]. It could also be due to a difference in the saturation efficiency between the two configurations [59, 60]. However, a full explanation of the increased transport in the Mirror configuration is beyond the scope of this study and left for future work.

4.2. Electron temperature effects on TEM turbulence

While simulations with artificial parameters can help to reduce the complexity of a system and isolate targeted physics, comparisons to experiments require matching experimental parameters as closely as possible. This section investigates how the TEM and quasi-stationary turbulence change when experimentally-relevant electron temperatures and gradients are simulated.

In section 3, and particularly figure 4, it was shown that there is significant variation in the normalized density and temperature gradients. While fluctuations and heat transport point to the importance of the density gradient, it is not uncommon for the temperature gradient to be larger than the density gradient at $r/a \approx 0.5$ in experimental profiles. The TEM can be destabilized by either a/L_n or a/L_{Te} , and the mixed gradients in experiment indicate that either gradient could be the dominant drive. When a temperature gradient $a/L_{Te} = 2$ is included in linear calculations, as in the top panel of figure 13, growth rates increase for all k_y . Additional gradient drive is added to the system and the linear instability is further destabilized, while the peak growth rate shifts slightly to higher k_y . However, growth rates of the dominant modes change in the same way for both the QHS and Mirror configurations, and do not predict any significant change to the comparison of configurations at $a/L_{Te} = 0$.

Previous simulations have used a temperature ratio $T_i/T_e = 1$, but electron temperatures in HSX are much larger than ion temperatures. At $r/a \approx 0.5$, the electron temperature of most profiles is 200–250 eV, while the ion temperature from CHERS measurements is 40–70 eV [34, 35]. Due to the lack of additional ion heating in HSX and the temperature dependence of the electron-ion collision frequency $\nu_{ei} \propto 1/T_e^{3/2}$, lower electron temperatures are generally associated with hotter ions, and the range of the temperature ratio at this radius is $0.15 \lesssim T_i/T_e \lesssim 0.35$. Simulations in this work use a baseline temperature ratio of $T_i/T_e = 0.2$ to represent the experiment. Linear calculations at this temperature ratio, on the bottom in figure 13, show that growth rates are reduced in both configurations for $k_y > 0.5$, but also that the divergence point between the QHS and Mirror growth rates shifts to higher k_y . With a unity temperature ratio, growth rates are larger in the QHS configuration for $k_y > 0.7$. When $T_i/T_e = 0.2$, the divergence point between the QHS and Mirror growth rates shifts to $k_y \approx 1.1$. Heat flux spectra in nonlinear simulations for HSX generally peak at $0.8 \lesssim k_y \lesssim 1$ (see spectra in figure 22), and the range $0.7 < k_y < 1.1$ covers a significant part of the wavenumbers most relevant to transport.

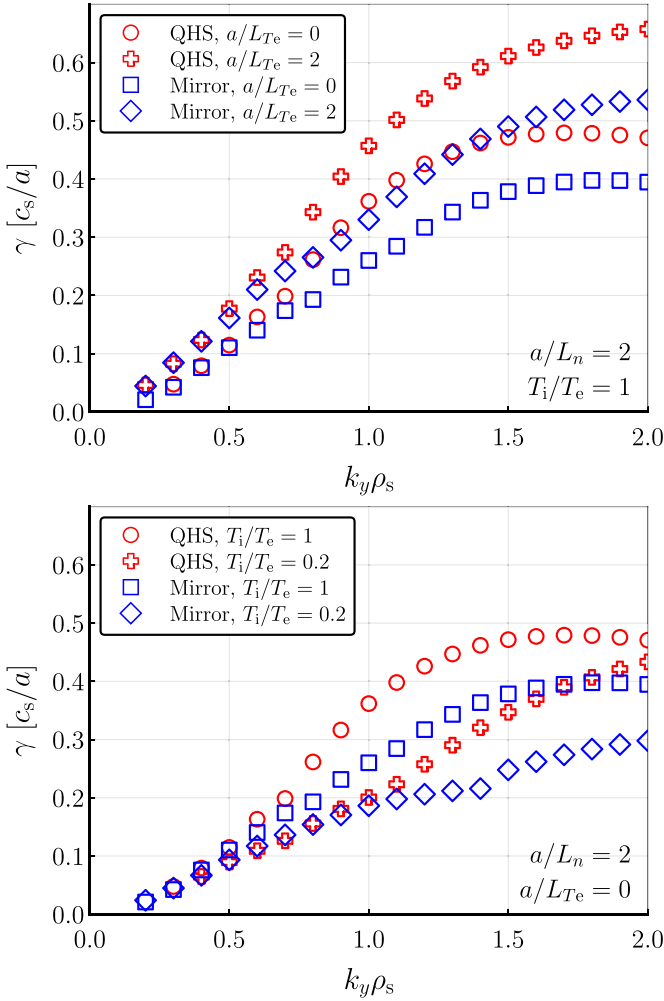


Figure 13. Linear growth rate spectra of the most unstable mode in the QHS and Mirror configurations when $a/L_n = 2$, showing the effect of finite a/L_{Te} (top) and non-unity T_i/T_e (bottom).

Fluxes from nonlinear simulations in figure 14 show that the difference of transport between QHS and Mirror configurations is reduced when using the experimentally relevant $T_i/T_e = 0.2$. This is despite the fact that the difference in heat flux at $T_i/T_e = 1$ is opposite to what would be expected from the difference in linear growth rates. Also note that the difference in the heat flux between configurations at $T_i/T_e = 1$ is much larger with the temperature gradient $a/L_{Te} = 2$ in figure 14, than with $a/L_{Te} = 0$ in figure 12. Within the expected range of temperature ratios $T_i/T_e < 0.4$, the temperature ratio does not have a large effect on transport in nonlinear simulations, and a large difference in experimental T_i/T_e between the QHS and Mirror configurations in HSX is not expected.

An improved quasilinear estimate of transport would often include coupling to other unstable eigenmodes [58]. The mode with the largest growth rate at a given wavenumber is the dominant mode. Particularly in stellarators, many other unstable modes may exist with a positive growth rate less than that of the dominant mode, known as subdominant modes. Such an estimate is outside the scope of this work, but the eigenspectrum of a number of subdominant modes is shown in figure 15.

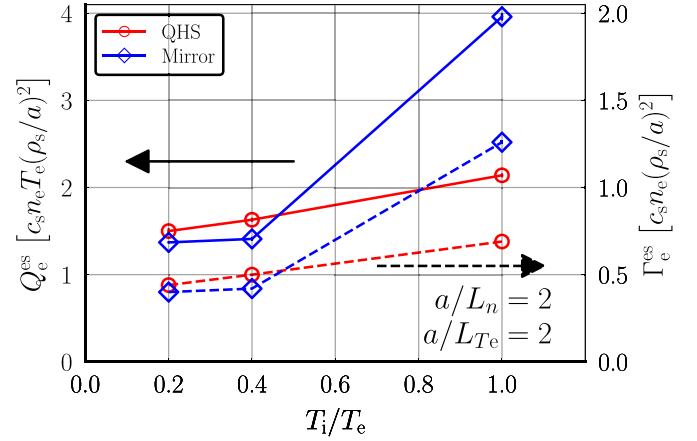


Figure 14. The heat flux (solid lines) and particle flux (dashed lines) from nonlinear simulations with changing temperature ratio T_i/T_e . Simulations here include both density and temperature gradient drives, $a/L_n = 2$ and $a/L_{Te} = 2$. Statistical error bars of the flux in the quasi-stationary state are indicated as vertical bars but are mostly smaller than the size of symbols.

As the temperature ratio is increased from $T_i/T_e = 0.2$ to $T_i/T_e = 1$, growth rates increase, as was seen in figure 13, and frequencies shift towards positive ω . At $T_i/T_e = 0.2$, all subdominant modes drift in the electron diamagnetic direction (negative ω), but at unity temperature ratio, a significant number of modes cross $\omega = 0$ and are drifting in the ion diamagnetic direction. These modes are likely the ubiquitous TEM [61], and were seen in previous QHS simulations at $T_i/T_e = 1$ [11]. Frequencies are involved in setting the nonlinear energy transfer efficiency, and it is possible that this frequency shift could change the relative contribution of modes involved in turbulence saturation. The contribution of frequencies has been investigated for the ITG mode in a quasi-symmetric configuration [59, 60], but has not yet been investigated for the TEM in stellarators. In addition, a transition of the most unstable mode is apparent in the QHS configuration. The most negative frequency mode, indicated by arrows in the top plot of figure 15, changes from dominant when $T_i/T_e = 1$ to subdominant when $T_i/T_e = 0.2$. The frequency shift away from the ion diamagnetic direction is also seen in frequencies from nonlinear simulations, even though nonlinear frequencies do not appear to match the frequency of any unstable linear mode in figure 15.

As the temperature ratio in simulation is decreased towards experimental values, the gradient scaling of linear growth rates changes significantly. Figures 16 and 17 compare contours of the linear growth rate as a function of a/L_n and a/L_{Te} for $k_y = 0.8$ at two different temperature ratios T_i/T_e . In figure 16, $T_i/T_e = 1$ and the growth rate of the TEM depends on both gradients, but somewhat more strongly on a/L_n , as expected for the ∇n -driven TEM. At small a/L_n , growth rates increase more quickly in QHS than in Mirror, but stagnate around $a/L_n \approx 2$ only in QHS. In figure 17, $T_i/T_e = 0.2$ and the growth-rate contours show that a/L_{Te} becomes the primary drive in significant parts of the investigated parameters space in both geometries. The increase of the growth rate is not

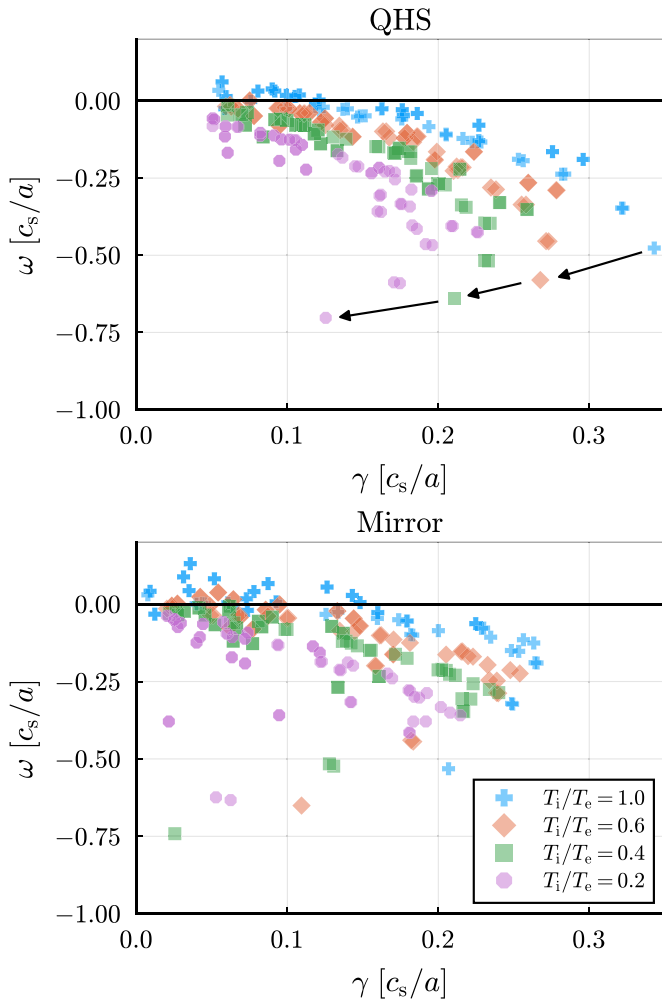


Figure 15. The inexhaustive eigenspectrum of subdominantly unstable modes in the QHS (top) and Mirror (bottom) configurations at $k_y = 0.8$ with $a/L_n = 2$ and $a/L_{Te} = 2$. The mode indicated by arrows in the top figure transitions from dominant to subdominant as T_i/T_e is reduced.

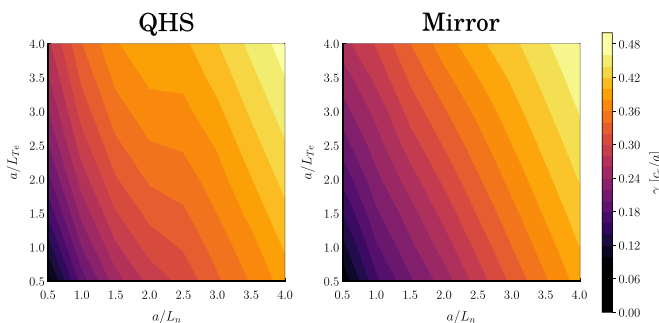


Figure 16. Contours of dominant TEM growth rates over a/L_n and a/L_{Te} for $k_y = 0.8$ at $T_i/T_e = 1$ in QHS (left) and Mirror (right).

monotonic with a/L_n in either configuration. This may be due to the exchange of the dominant unstable mode with a subdominant one that depends more strongly on the temperature gradient instead of the density gradient. This transition happens at a smaller a/L_n in QHS than in Mirror, and there may be a range of gradients where the gradient dependence of the TEM in the

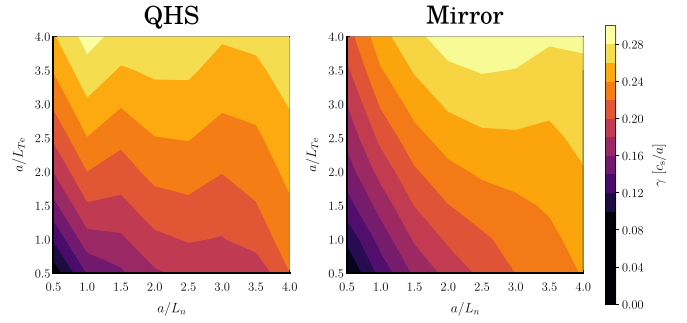


Figure 17. Contours of dominant TEM growth rates over a/L_n and a/L_{Te} for $k_y = 0.8$ at $T_i/T_e = 0.2$ in QHS (left) and Mirror (right). Note the different color bar relative to figure 16.

two configurations diverges. The correct temperature ratio is important to capture the gradient trend of linear growth rates, and may influence nonlinear simulations similarly.

4.3. TEM simulations at experimental gradients

Simulated turbulent fluxes can vary dramatically when accounting for the experimental uncertainties of measured gradients, which can cause comparisons to misleadingly identify a difference between experiment and simulation. The gradients in simulation can be varied across the uncertainty of the gradient measurement to match the experimental flux in the quasi-stationary state. Further comparisons can investigate whether the underlying turbulence in this matched simulation reproduces experimental measurements. To this end, this section provides scans of gradients across the experimental distribution to compare how the heat flux scales with gradients. Simulations here fix one gradient and scan either the density gradient or temperature gradient. The values of the gradients covered are based on the distribution of experimental gradients in figure 4.

While figures 11 and 16 show that dominant linear growth rates depend strongly on the density gradient at the artificial $T_i/T_e = 1$, figure 17 shows that the situation is different at $k_y = 0.8$ when $T_i/T_e = 0.2$ as in experiment. For $a/L_n \approx 2$, growth rates are expected to scale only weakly with the density gradient. The linear growth rates in figure 18 confirm this weak scaling with a/L_n . The Mirror configuration has reduced growth rates for $k_y > 1$, but the difference between QHS and Mirror for $k_y < 1$ is minimal, as demonstrated in figure 13. Analysis of subdominant modes at $k_y = 0.8$ does not identify any large change in eigenspectra with changing density gradient.

The heat flux is plotted for nonlinear simulations scanning the density gradient in figure 19. As the density gradient increases from $a/L_n = 2$ to 2.5, the heat flux increases steeply by a factor of about 2.5. This increase in transport raises the possibility that the ∇n -driven TEM could be limiting the maximum achievable profile gradients at this location in both the QHS and Mirror configurations. When comparing to the experimental data, very few profiles have density gradients larger than $a/L_n = 2.5$ in figure 4. However, more nonlinear simulations are needed to understand if the flux is a function of a/L_n or $\eta_e = L_n/L_{Te}$ in order to compare to the

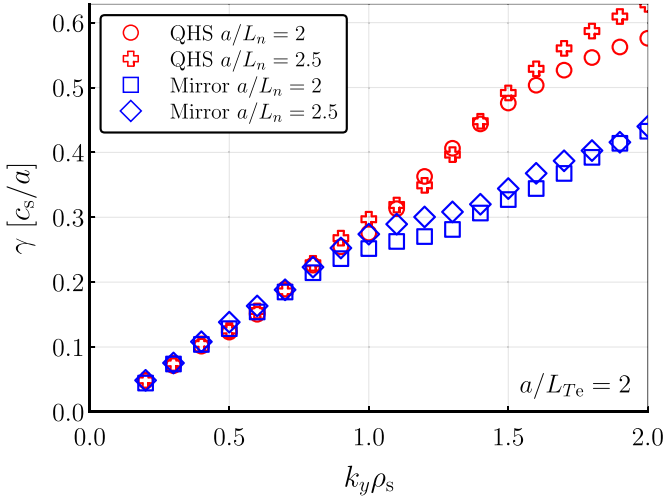


Figure 18. Spectra of linear growth rates with increasing a/L_n for $a/L_{Te} = 2$, $T_i/T_e = 0.2$ in the QHS (red) and Mirror (blue) configurations.

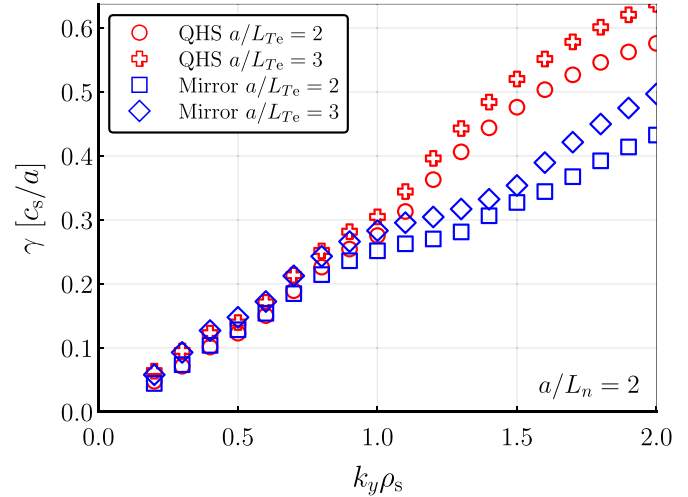


Figure 20. Linear growth rates for $a/L_n = 2$ and $T_i/T_e = 0.2$ in the QHS (red) and Mirror (blue) configurations, for two different a/L_{Te} .

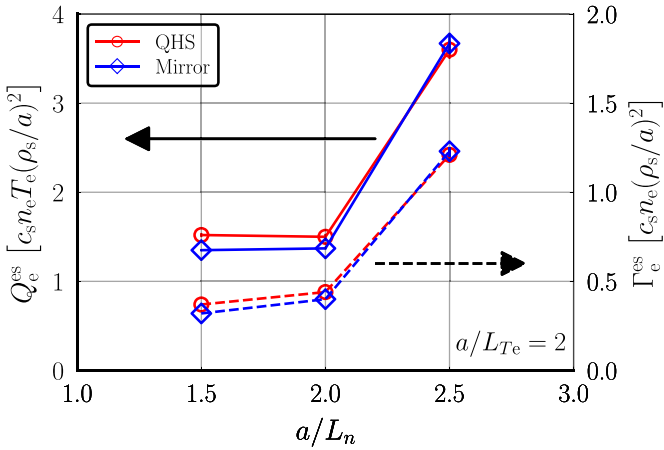


Figure 19. The nonlinear heat flux (solid lines) and particle flux (dashed lines) for simulations scanning a/L_n with $a/L_{Te} = 2$ and $T_i/T_e = 0.2$ in the QHS (red circle) and Mirror (blue diamond) configurations. Statistical error bars of the flux in the quasi-stationary state are indicated as vertical bars but are mostly smaller than the size of symbols.

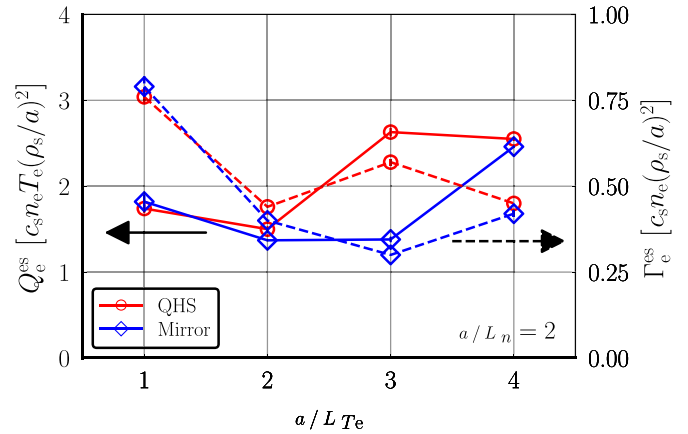


Figure 21. The nonlinear heat flux Q_e^{es} (solid lines) and particle flux Γ_e^{es} (dashed lines) for simulations scanning a/L_{Te} with $a/L_n = 2$ and $T_i/T_e = 0.2$. Statistical error bars of the flux in the quasi-stationary state are indicated as vertical bars but are mostly smaller than the size of symbols.

distribution of experimental profiles. While linear growth rates in figure 18 increase slightly with density gradient, there is no sudden change in growth rates similar to the steep change in heat flux. At the high k_y , where QHS and Mirror do differ, the usual quasilinear expectation $Q \propto \gamma/k_y^2$ would suggest that these modes contribute only slightly to the nonlinear heat flux. Differences between the QHS and Mirror configuration in nonlinear simulation are small and not measurable in the experiment.

As seen in figure 20, increasing the temperature gradient increases growth rates proportionally across all k_y , as expected from figures 13 and 17. Similar to figure 18, growth rates do not differ significantly between QHS and Mirror for the range of transport-relevant wavenumbers $k_y < 1$. The eigen-spectrum (not shown) demonstrates that growth rates increase for all subdominant modes, but no frequency shift or change

in dominant mode is found. However, the transport in nonlinear simulations scanning the temperature gradient, shown in figure 21, does not show any straightforward trend with temperature gradient. Particularly at $a/L_{Te} = 3$, where linear growth rates in figure 20 increase similarly for both the QHS and Mirror configuration, the heat flux increases in QHS but not in Mirror. In addition, the heat and particle fluxes do not scale similarly with the temperature gradient. While the temperature gradient is larger than the density gradient, the heat flux roughly increases with increasing a/L_{Te} , whereas the particle flux is significantly less sensitive. Both fluxes increase when the temperature gradient is smaller than the density gradient, but the increase in particle flux is much larger. The density-potential and temperature-potential cross phases in the transport-relevant wavenumber range show no strong shifts across the gradient scans, and the different trends of the heat and particle fluxes are directly related to different fluctuation amplitudes in the simulations. These results

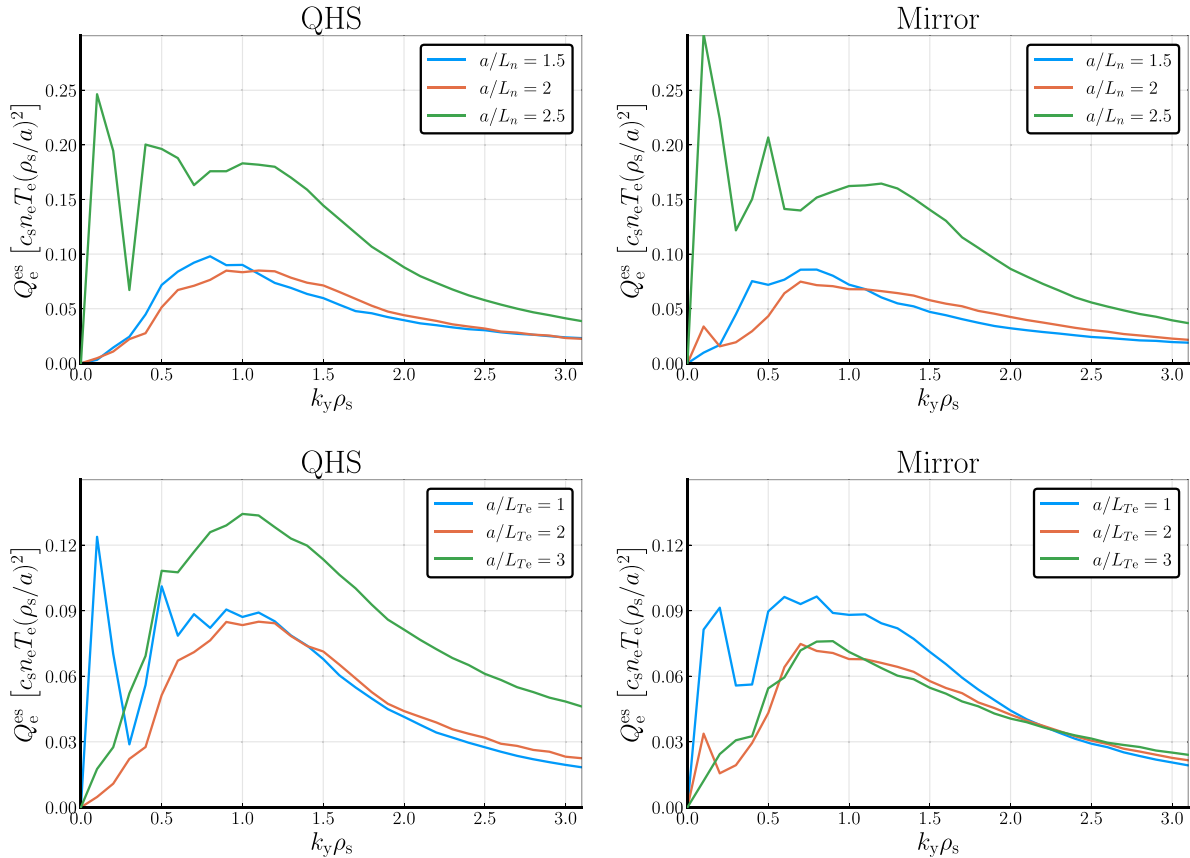


Figure 22. Heat flux spectra from nonlinear simulations in the QHS (left column) and Mirror (right column) configurations for density gradient scans at $a/L_n = 2$ (top row) and temperature gradient scans at $a/L_n = 2$ (bottom row). Note the different y-axis in upper and lower plots.

show that the particle flux may in fact be reduced by increasing a/L_{Te} . Crossing $a/L_n = a/L_{Te}$ results in a change of the dominant gradient-drive, which is associated here with different sensitivities to the gradient.

Heat flux spectra and frequency spectra from nonlinear simulations both show shifts sensitive to the changing gradients, possibly highlighting a change in the nonlinear dynamics. Spectra of the heat flux from nonlinear simulations, presented in figure 22, show that the bulk of transport is driven by modes around $k_y \approx 1$, but the magnitude of a low- k_y peak is sensitive to a/L_n and a/L_{Te} . The bulk peak flux shifts to higher wavenumbers as the density gradient increases, but does not shift significantly with increasing temperature gradient. Nonlinear simulations in [11] with $T_i/T_e = 1$ previously identified a low- k_y feature in the flux spectra of the QHS configuration, which also appears in figure 22 for the present simulations in QHS and Mirror with finite a/L_{Te} and $T_i/T_e = 0.2$. The low- k_y peak does not depend solely on a/L_n , but rather increases in magnitude with increasing ratio of a/L_n to a/L_{Te} , and is more pronounced in the Mirror configuration. As discussed in [11], this feature is well resolved numerically and, for realistic gradients, is narrow and does not correspond to a substantial fraction of the total flux. However, it may have an effect on coupling between modes and the overall saturation level. A greater understanding of the low- k_y peak and its implications is left for future work.

In figure 21, transport increases with a/L_{Te} above $a/L_{Te} = a/L_n$, but much more weakly than the dependence on the density gradient in figure 19. In the QHS configuration, the dependence of the heat flux on the temperature gradient between $a/L_{Te} = 2$ and 3 is weaker than the dependence on the density gradient between $a/L_n = 2$ and 2.5 by a factor of three. Linear growth rates in figure 18 predicted no change with density gradient, while growth rates in figure 20 increase with a/L_{Te} . Instead, the nonlinear heat flux is more sensitive to the density gradient.

The frequency spectra in figure 23 suggest a qualitative change in the turbulence as the density gradient is increased, possibly explaining the discrepancy between linear growth rates and nonlinear heat flux. When $a/L_n \leq a/L_{Te}$, a distinct negative-frequency band exists up to $k_y \approx 1.5$, which covers the range of wavenumbers responsible for most transport. In [11], this band was associated with TEMs. However, as the density gradient is increased, this band of negative frequencies recedes to small k_y , and is replaced by a wide positive frequency band. For $a/L_n > a/L_{Te}$, frequencies in the nonlinear simulation are broadly positive for all k_y . Increasing a/L_n has a similar effect on the nonlinear frequencies as decreasing a/L_{Te} or decreasing T_i/T_e .

Heuristically, scaling with driving gradients is sensitive to whether the negative-frequency or positive-frequency turbulence is responsible for transport. The transition between

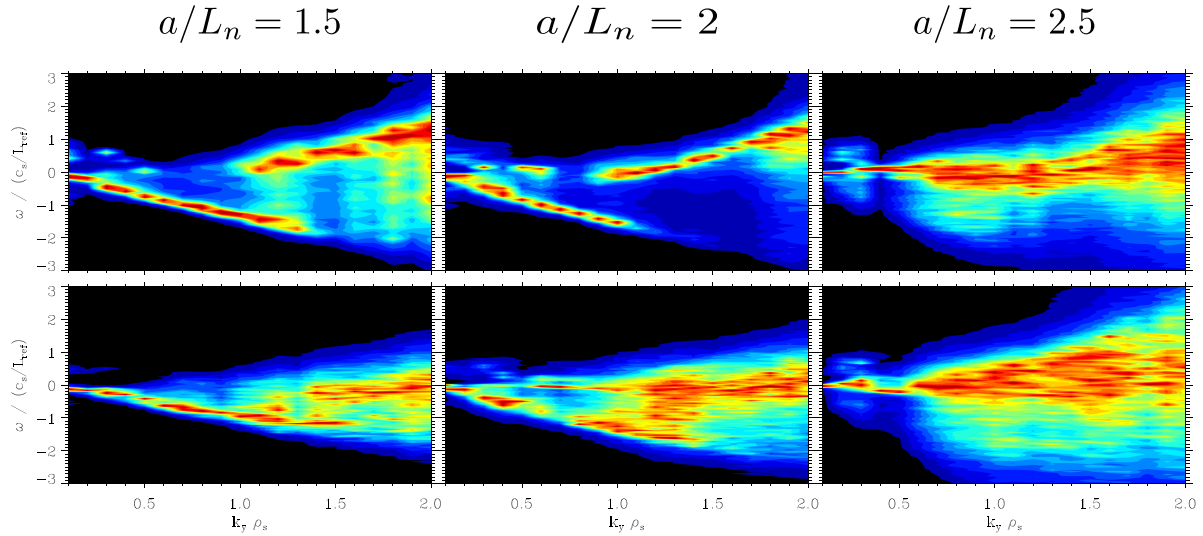


Figure 23. Frequencies based on potential data from nonlinear simulations in QHS (top) and Mirror (bottom) with $a/L_{Te} = 2$, $T_i/T_e = 0.2$, and changing a/L_n . The color scale is linear and independently scaled for each k_y .

regimes is not surprising, as the experimental gradients lie at the transition between a/L_n and a/L_{Te} drive, which, based on figure 21 may be a preferred state of lower flux. However, the uncertainty in profile gradients in figure 4 is large enough that the dominant gradient drive cannot be determined with certainty in most of the studied discharges.

The different scaling of the heat flux in these two regimes may be important for profile shapes in HSX. It is possible that the electron thermal diffusivity could be a function of L_n/L_{Te} , and the stiffness of thermal transport in the ∇T_e -driven regime may be reduced as compared to the ∇n -driven regime. In that case, a larger electron temperature gradient could be supported when $\eta_e < 1$ than when $\eta_e > 1$.

5. Comparison of simulation and experiment

While lacking the rigorous metrics of a strict validation study [5, 62], comparison of the measurements in section 3 to simulations in section 4.3 can identify the necessary steps to make proper validation possible, such as more precise measurements or simulations more accurately matched to experimental conditions. TEM simulations use a local flux-tube domain centered at the $r/a = 0.7$ surface, while measurements are from $r/a = 0.5$. The low shear in HSX means that the geometry does not change much between surfaces, but it is not clear *a priori* how strongly geometry needs to be modified before nonlinear dynamics are altered. Results with a zero-shear approximation [8] provide confidence that any change in shear due to the different radial location is unlikely to affect the instability drive significantly. Also, the flux-tube simulation domain is a reduced-geometry representation that, among other limitations, can not include a radial electric field. Ambipolar radial electric fields may drive flows that shift turbulence on the flux surface, lead to shear stabilization, or interact with zonal flows. As a radially-local representation, the flux tube may not account for profile effects on the order of the

width of zonal flows, which could be important for turbulence saturation.

5.1. Simulated heat flux compared to experimental power balance

In section 3.1, it was found that the experimental energy transport is larger in Mirror than in QHS at the mid-radius when the gradient drive is matched between configurations. This is demonstrated by the larger heat flux in figure 6 and the matched heat flux at smaller a/L_n in the temperature gradient scaling in figure 7. This difference in transport is not reproduced in simulations at the experimental temperature ratio T_i/T_e . However, fluxes are sensitive to whether turbulence is in the ∇n -driven or ∇T_e -driven regime. Small changes in gradient may change the dominant drive and cause significant changes in flux. In section 4.2, simulations with temperature ratio $T_i/T_e = 1$ do produce a larger heat flux in the Mirror configuration, and decreasing T_i/T_e has a similar effect on the nonlinear frequencies as increasing a/L_n . If changing the temperature ratio is similar to scanning gradients between the ∇n -driven and ∇T_e -driven regimes, it is possible the QHS and Mirror heat flux in simulation may diverge with further exploration of higher gradients. However, higher gradients are not represented in the experimental data in figure 4, and more precise gradient measurements will be required to show a configurational dependence of the TEM in HSX.

However, nonlinear simulations do reproduce the general gradient dependence of the TEM turbulence in HSX. In both simulation and experiment, the electron heat flux increases more strongly with the density gradient than the temperature gradient. The normalization of the electron heat flux from simulation depends on the background density and electron temperature. However, the experimental data represents a number of different discharges with a range of plasma profiles. The distribution of densities and temperatures in the selection of experimental profiles is accounted for as uncertainty

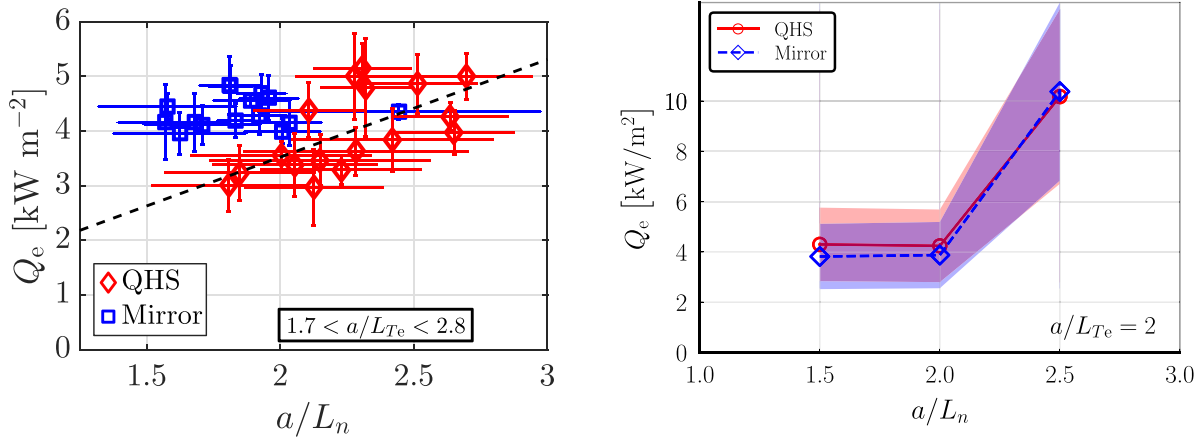


Figure 24. The heat flux increases with increasing density gradient a/L_n in both experimental measurements (left) and GENE simulations (right). The shaded uncertainty on the right comes from the distribution of electron temperatures and densities (but not their gradients) for the experimental profiles represented in the experimental data on the left. The statistical uncertainty of individual nonlinear simulations is comparatively negligible.

of the normalization parameters. As seen in figure 24, the electron heat flux from simulation of TEM turbulence does account for the heat flux in experimental discharges, being about 4 kW m^{-2} in both cases. These comparisons strongly suggest that TEM turbulence is the dominant driver of anomalous transport in HSX. The electron heat flux increases sharply for the simulation with a larger density gradient, up to 10 kW m^{-2} . While the experimental data does not show a steep increase for $a/L_n > 2$, it is not known how the range of a/L_{Te} in the experimental data would affect the simulated nonlinear fluxes. Between the large experimental gradient uncertainties and the small number of nonlinear simulations, it is hard to say whether the steep increase in flux is compatible with the experimental data. It is possible that this strong boost of the TEM turbulence may be responsible for limiting the achievable gradients in the experiment, and may explain the lack of profiles with $a/L_n > 2.5$ in figure 4. Identification of the specific gradients at which this transition happens in the simulations of the QHS and Mirror configurations may explain the typically larger density gradient in the QHS configuration. In addition, the weaker dependence on the temperature gradient in figure 7 may explain the broader range $0 \lesssim a/L_{Te} \lesssim 4$ of that gradient in experimental data.

5.2. Density fluctuation amplitude compared to reflectometry

Density fluctuations are a local quantity, and comparison between simulation and experiment is sensitive to the precise location of measurement, as was exploited in [16]. In a stellarator, each flux tube on a surface is unique, and it is not guaranteed that a given observation volume will overlap with the computational domain. The HSX reflectometer is positioned on the outboard mid-plane of the bean-shaped cross section, which is precisely the midpoint of the flux tube used in the present simulations. For a probe beam perpendicular to the surface and small-amplitude density fluctuations, most of the reflected power comes from the vicinity of the

probing beam axis. As a first-order comparison to experiment, the reflectometer measurement volume is taken to be only the $z=0$ midpoint of the flux tube, with fluctuations measured in the range $0.2 \lesssim k_{\perp} \rho_s \lesssim 1$. In reality, the diagnostic has some instrument function that determines the response to fluctuations at a given wavenumber. However, for the analysis here, the density fluctuation spectrum is integrated across the given k_{\perp} range. The conversion to GENE wavenumbers depends on geometric coefficients as $k_{\perp}^2 = g^{xx}k_x^2 + 2g^{xy}k_xk_y + g^{yy}k_y^2$ [63]. At the midpoint of the flux tube on the stellarator symmetry plane, where the reflectometer measurement is located, $g^{xy} = 0$. Therefore, $k_{\perp} = \sqrt{g^{xx}k_x^2 + g^{yy}k_y^2}$, with $g^{xx} = 2.98$ and $g^{yy} = 0.381$ in QHS, and $g^{xx} = 2.55$ and $g^{yy} = 0.320$ in Mirror. This approximation of an instrument function is only the first step of a synthetic diagnostic but makes application to simulation data straightforward.

The results of this analysis are shown next to experimental measurements in figure 25. To compare simulated fluctuations to experimental measurements, the normalization factor of ρ_s/a must be included. The reflectometer measurements in figure 25 come from plasma profiles with a distribution of electron temperatures. The plotted uncertainty on simulated fluctuation amplitudes comes from this distribution through the temperature dependence of ρ_s . There is not enough experimental data in figure 25(left) to differentiate between the QHS and Mirror configurations, but no substantial difference is expected from GENE simulations (right). Any configuration effect on density fluctuation amplitude would be smaller than the scatter in the experimental parameters of this sample, and so the the QHS and Mirror data can be assessed in aggregate. In both simulation and experiment, density fluctuations increase with increasing density gradient. This mirrors the scaling of the heat flux, and indicates that density fluctuations are a good indicator of the amplitude of ∇n -driven TEM turbulence. While density fluctuations from simulation have a larger amplitude than fluctuations measured by reflectometry, the absolute value of density fluctuations from both the experiment and simulation

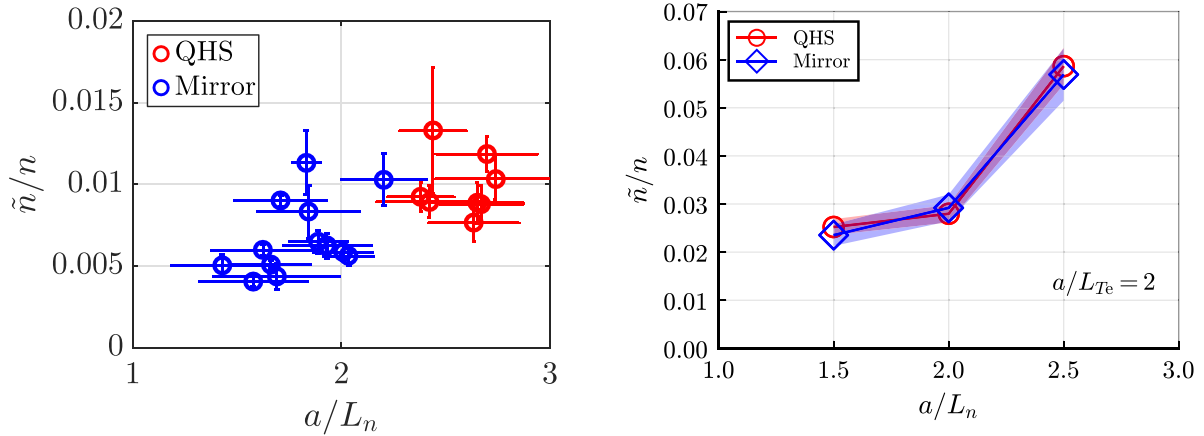


Figure 25. When considering data from both configurations, the density fluctuation amplitude increases with increasing density gradient a/L_n in both reflectometer measurements (left) and GENE simulations (right). The shaded uncertainty for simulated fluctuations on the right comes from the distribution of electron temperatures for the experimental profiles represented in the reflectometer data ($1.8 < a/L_{Te} < 3.1$).

should be interpreted with caution. As discussed in section 3.2, the model for density fluctuations is only intended to enable the comparison of the dependence of fluctuation amplitudes on the gradient between configurations. In addition, the approach described in this section is only a first-order approach to a synthetic diagnostic. This comparison of density fluctuations in simulation and experiment is encouragement for the future development of a detailed synthetic diagnostic.

6. Summary

In this study, the magnetic configuration flexibility of the HSX has been used to investigate trapped-electron-mode turbulence in quasi-helically symmetric and degraded-symmetry configurations, including a detailed comparison of experimental measurements to nonlinear gyrokinetic simulations of trapped-electron-mode turbulence at experimental parameters. The simulated nonlinear heat flux increases more strongly with a/L_n , but linear growth rates increase more strongly with a/L_{Te} . While the linear growth rate of the most unstable mode is not predictive of overall turbulence, it was shown that key experimental trends are captured in nonlinear simulations. The simulated heat flux matches measurements within experimental uncertainties for both configurations, and the heat flux scales more strongly with the density gradient than the temperature gradient in both simulation and experiment. At higher density gradients, the simulated heat flux increases dramatically, suggesting that ∇n -driven TEM turbulence may be responsible for limiting the achievable density gradients in the experiment. A comparison of density fluctuations finds that simulated density fluctuations increase with density gradient but are independent of the temperature gradient, in agreement with measurements. Fluctuation amplitudes from simulation are larger than experimental measurements, but a quantitative comparison requires more development of the fluctuation model and synthetic diagnostic. The matched heat flux and gradient drive between simulation and experiment indicate that ∇n -driven TEM turbulence is the dominant driver of anomalous

transport at the mid-radius in HSX. The results of the comparison between simulation and experiment are summarized here:

- The magnitude of the heat flux $Q_e \approx 4 \text{ kW m}^{-2}$ in both simulation and experiment.
- Q_e depends more strongly on a/L_n than a/L_{Te} in both simulation and experiment.
- In the experiment, the Mirror heat flux is larger than QHS, but this is not reproduced in simulation at $T_i/T_e = 0.2$.
- Density fluctuation amplitude increases with increasing a/L_n in both simulation and experiment.
- Density fluctuation amplitudes are larger in simulation than experimental measurements but require validation of the fluctuation model and synthetic diagnostic approximations.

While simulations at experimental parameters do not predict the difference in heat flux between configurations, the heat flux is sensitive to whether turbulence is in the ∇n -driven or ∇T_e -driven regime, and more precise profile gradient measurements are required. Frequencies in nonlinear simulations transition from the electron diamagnetic direction when $a/L_{Te} > a/L_n$ to the ion direction when $a/L_n > a/L_{Te}$, despite the absence of strongly unstable linear modes with a positive frequency. These findings suggest that the dynamics of the TEM are substantially affected by nonlinear effects, as opposed to following a simple quasi-linear trend. As this change occurs around $a/L_n = a/L_{Te}$, the density and temperature gradient drives are potentially associated with different saturation levels and nonlinear dynamics in the quasi-stationary state. This transition differs between the QHS and Mirror configurations, with positive frequencies appearing earlier with increasing a/L_n in the QHS configuration than in Mirror, and is affected by decreasing the temperature ratio in a similar way to increasing the density gradient.

Measurements of fluctuation frequencies may be a valuable indicator of turbulence regime. While the HSX reflectometer cannot measure the phase velocity in the ion or electron direction, the positive frequencies are associated with a broader

spectrum. Previous analysis of reflectometry shows that frequency spectra are much broader in the Mirror configuration, and that a coherent mode is detected in QHS [42, 64]. It would be worthwhile to understand if this comparison changes with driving gradients, and if it can be explained by TEM turbulence simulation.

Data availability statement

The data cannot be made publicly available upon publication because they are not available in a format that is sufficiently accessible or reusable by other researchers. The data that support the findings of this study are available upon reasonable request from the authors.

Acknowledgments

The authors gratefully acknowledge discussions with J H E Proll, T Windisch, M J Gerard, J C Schmitt, P W Terry, and C C Hegna. This research was supported by funding from U.S. Department of Energy Grants DE-FG02-93ER54222 and DE-FG02-04ER-54742 and used resources of the National Energy Research Scientific Computing Center (NERSC), a U.S. Department of Energy Office of Science User Facility operated under Contract No. DE-AC02-05CH11231.

ORCID iDs

J Smoniewski  0000-0002-4028-826X
 G M Weir  0000-0002-2370-409X
 M J Pueschel  0000-0003-3895-1920
 B J Faber  0000-0003-4934-400X
 I J McKinney  0000-0001-6213-7238
 H Hillebrecht  0000-0002-8682-235X
 B Geiger  0000-0001-8706-1874

References

- [1] Kick M, Maaßberg H, Anton M, Baldzuhn J, Endler M, Görner C, Hirsch M, Weller A and Zoletnik S 1999 *Plasma Phys. Control. Fusion* **41** A549
- [2] Canik J M, Anderson D T, Anderson F S B, Likin K M, Talmadge J N and Zhai K 2007 *Phys. Rev. Lett.* **98** 085002
- [3] Beidler C D et al 2021 *Nature* **596** 221
- [4] Mynick H E, Pomphrey N and Xanthopoulos P 2010 *Phys. Rev. Lett.* **105** 095004
- [5] Terry P W, Greenwald M, Leboeuf J N, McKee G R, Mikkelsen D R, Nevins W M, Newman D E and Stotler D P 2008 *Phys. Plasmas* **15** 062503
- [6] Greenwald M 2010 *Phys. Plasmas* **17** 058101
- [7] White A E 2019 *J. Plasma Phys.* **85** 745850101
- [8] Faber B J, Pueschel M J, Terry P W, Hegna C C and Roman J E 2018 *J. Plasma Phys.* **84** 905840503
- [9] Tanaka K et al 2020 *Plasma Phys. Control. Fusion* **62** 024006
- [10] Tanaka K et al 2021 *Plasma Phys. Control. Fusion* **63** 094001
- [11] Faber B J, Pueschel M J, Proll J H E, Xanthopoulos P, Terry P W, Hegna C C, Weir G M, Likin K M and Talmadge J N 2015 *Phys. Plasmas* **22** 072305
- [12] Proll J H E, Mynick H E, Xanthopoulos P, Lazerson S A and Faber B J 2016 *Plasma Phys. Control. Fusion* **58** 014006
- [13] Stroteich S, Xanthopoulos P, Plunk G and Schneider R 2022 *J. Plasma Phys.* **88** 175880501
- [14] Weir G M, Faber B J, Likin K M, Talmadge J N, Anderson D T and Anderson F S B 2015 *Phys. Plasmas* **22** 056107
- [15] Alcusón J et al 2023 *Nucl. Fusion* **63** 094002
- [16] Sanchez E, Estrada T, Velasco J L, Calvo I, Cappa A, Alonso J A, García-Regana J M, Kleiber R and Riemann J 2019 *Nucl. Fusion* **59** 076029
- [17] Coelho A J, Loizu J, Ricci P, Ramisch M, Köhn-Seemann A, Birkenmeier G and Rahbarnia K 2023 *Plasma Phys. Control. Fusion* **65** 085018
- [18] Jenko F, Dorland W, Kotschenreuther M and Rogers B N 2000 *Phys. Plasmas* **7** 1904
- [19] Anderson F S B, Almagri A F, Anderson D T, Matthews P G, Talmadge J N and Shohet J L 1995 *Fusion Technol.* **27** 273
- [20] Boozer A H 1983 *Phys. Fluids* **26** 496
- [21] Nührenberg J and Zille R 1988 *Phys. Lett. A* **129** 113
- [22] Canik J M, Anderson D T, Anderson F S B, Clark C, Likin K M, Talmadge J N and Zhai K 2007 *Phys. Plasmas* **14** 056107
- [23] Stroth U, Murakami M, Dory R A, Yamada H, Okamura S, Sano F and Obiki T 1996 *Nucl. Fusion* **36** 1063
- [24] Gerhardt S P, Talmadge J N, Canik J M and Anderson D T 2005 *Phys. Rev. Lett.* **94** 015002
- [25] Watanabe T H, Sugama H and Ferrando-Margalet S 2008 *Phys. Rev. Lett.* **100** 195002
- [26] Rafiq T and Hegna C C 2005 *Phys. Plasmas* **12** 112505
- [27] Guttenfelder W, Lore J, Anderson D T, Anderson F S B, Canik J M, Dorland W, Likin K M and Talmadge J N 2008 *Phys. Rev. Lett.* **101** 215002
- [28] Gerard M J, Pueschel M J, Geiger B, Mackenbach R J J, Duff J M, Faber B J, Hegna C C and Terry P W 2024 *Phys. Plasmas* **31** 052501
- [29] Guttenfelder W A 2008 Measurements and Modeling of Turbulent Transport in the HSX Stellarator *PhD Thesis* The University of Wisconsin-Madison
- [30] Guttenfelder W, Anderson D T, Anderson F S B, Canik J M, Likin K M and Talmadge J N 2009 *Phys. Plasmas* **16** 082508
- [31] Zhai K, Anderson F S B, Willis K, Likin K and Anderson D T 2004 *Rev. Sci. Instrum.* **75** 3900
- [32] Goodman W R, Scott E R, Keith Z, Singh L and Anderson D T 2022 *Rev. Sci. Instrum.* **93** 093518
- [33] Chilenski M A, Greenwald M, Marzouk Y, Howard N T, White A E, Rice J E and Walk J R 2015 *Nucl. Fusion* **55** 023012
- [34] Briesemeister A, Zhai K, Anderson D T, Anderson F S B and Talmadge J N 2013 *Plasma Phys. Control. Fusion* **55** 014002
- [35] Kumar S T A, Dobbins T J, Talmadge J N, Wilcox R S and Anderson D T 2018 *Plasma Phys. Control. Fusion* **60** 054012
- [36] Weir G M, Likin K M, Marushchenko N B and Turkin Y 2015 *Nucl. Fusion* **55** 113011
- [37] Lore J, Guttenfelder W, Briesemeister A, Anderson D T, Anderson F S B, Deng C B, Likin K M, Spong D A, Talmadge J N and Zhai K 2010 *Phys. Plasmas* **17** 056101
- [38] Spong D A 2005 *Phys. Plasmas* **12** 056114
- [39] Lore J D 2010 Measurement and transport modeling with momentum conservation of an electron internal transport barrier in HSX *PhD Thesis* The University of Wisconsin-Madison
- [40] Estrada T et al 2021 *Nucl. Fusion* **61** 046008
- [41] González-Jerez A, García-Regana J, Calvo I, Carralero D, Estrada T, Sánchez E and Barnes M (the W7-X Team) 2024 *Nucl. Fusion* **64** 076029
- [42] Likin K M, Lechte C, Lu H and Anderson F S B 2007 ECE and reflectometry on the helically symmetric experiment *Proc. ITC/ISHW2007*

- [43] Stix T H 1992 *Waves in Plasmas* (American Institute of Physics Melville)
- [44] Gusakov E Z and Popov A Y 2002 *Plasma Phys. Control. Fusion* **44** 2327
- [45] Happel T, Görler T, Hennequin P, Lechte C, Bernert M, Conway G D, Freethy S J, Honoré C, Pinzón J R and Stroth U (The ASDEX Upgrade Team) 2017 *Plasma Phys. Control. Fusion* **59** 054009
- [46] Conway G D 1999 *Plasma Phys. Control. Fusion* **41** 65
- [47] Conway G D, Schott L and Hirose A 1996 *Rev. Sci. Instrum.* **67** 3861
- [48] Xanthopoulos P, Cooper W A, Jenko F, Turkin Y, Runov A and Geiger J 2009 *Phys. Plasmas* **16** 082303
- [49] Hirshman S P and Whitson J C 1983 *Phys. Fluids* **26** 3553
- [50] Beer M A, Cowley S C and Hammett G W 1995 *Phys. Plasmas* **2** 2687
- [51] Grimm R C, Greene J M and Johnson J L 1976 Computation of the magnetohydrodynamic spectrum in axisymmetric toroidal confinement systems *Methods in Computational Physics: Advances in Research and Applications (Controlled Fusion)* vol 16 (Elsevier) pp 253–80
- [52] Smoniewski J, Sánchez E, Calvo I, Pueschel M J and Talmadge J N 2021 *Phys. Plasmas* **28** 042503
- [53] Martin M F, Landreman M, Xanthopoulos P, Mandell N R and Dorland W 2018 *Plasma Phys. Control. Fusion* **60** 095008
- [54] Xanthopoulos P, Plunk G G, Zocco A and Helander P 2016 *Phys. Rev. X* **6** 021033
- [55] Deng C B, Brower D L, Anderson D T, Anderson F S B, Briesemeister A and Likin K M 2015 *Nucl. Fusion* **55** 123003
- [56] Casati A *et al* 2009 *Nucl. Fusion* **49** 085012
- [57] McKinney I J, Pueschel M J, Faber B J, Hegna C C, Talmadge J N, Anderson D T, Mynick H E and Xanthopoulos P 2019 *J. Plasma Phys.* **85** 905850503
- [58] Pueschel M J, Faber B J, Citrin J, Hegna C C, Terry P W and Hatch D R 2016 *Phys. Rev. Lett.* **116** 085001
- [59] Terry P W, Faber B J, Hegna C C, Mirnov V V, Pueschel M J and Whelan G G 2018 *Phys. Plasmas* **25** 012308
- [60] Hegna C C, Terry P W and Faber B J 2018 *Phys. Plasmas* **25** 022511
- [61] Coppi B, Migliuolo S and Pu Y K 1990 *Phys. Fluids B* **2** 2322
- [62] Holland C 2016 *Phys. Plasmas* **23** 060901
- [63] Told D 2012 Gyrokinetic microturbulence in transport barriers *PhD Thesis* Universität Ulm
- [64] Han X, Richardson M, Likin K M, Hillebrecht H O M, Geiger B, Goodman W, Wolfmeister A, Knowles B and Wagner R (the HSX Team) 2025 *Plasma Phys. Control. Fusion* **67** 045011